CHAPTER

16

Computational Modeling and Simulation of Animal Early Embryogenesis with the MecaGen Platform

Julien Delile[a,c], *René Doursat*[a,b], *Nadine Peyriéras*[c]

[a]Institut des Systèmes Complexes Paris Ile-de-France (ISC-PIF), CNRS, Paris, France
[b]School of Biomedical Engineering, Drexel University, Philadelphia, PA, USA
[c]Neurobiology and Development Lab, Terrasse, Gif-sur-Yvette Cedex, France

CONTENTS

http://dx.doi.org/10.1016/B978-0-12-405926-9.00016-2

Abstract

We propose a theoretical, yet realistic agent-based model and simulation platform of animal embryogenesis, called MecaGen,[1] centered on the physico-chemical coupling of cell mechanics with gene expression and molecular signaling. This project aims to investigate the multiscale dynamics of the early stages of biological morphogenesis. Here, embryonic development is viewed as an emergent, self-organized phenomenon based on a myriad of cells and their genetically regulated, and regulating, biomechanical behavior. Cells' mechanical properties (such as division rate, adhesion strength, or intrinsic motility) are closely correlated with their spatial location and temporal state of genetic and molecular dynamics (such as internal protein and external ligand concentrations) and affect each other concurrently. In a second part, we illustrate our model on artificial data (gene regulation motifs and cell sorting), then demonstrate a customization and application to a real biological case study in the zebrafish early development. We use as an example the episode of intercalation patterns appearing during the first phase of epiboly and the movements of the deep cells between the yolk and the enveloping layer. A domain of the model's multidimensional parameter space is explored systematically, while experimental data obtained from microscopy imaging of live embryos is used to measure the "fitness" of the virtual embryo and validate our hypotheses.

1 INTRODUCTION

The spontaneous making of an entire multicellular organism from a single cell ranks among the most exquisitely complex phenomena in nature. Through a precise spatiotemporal interplay of genetic switches, chemical signals, and mechanical constraints, an elaborate form is created without any of its myriad of cells containing the explicit map of the resulting architecture. An eternal source of fascination for generations of philosophers, artists, and scientists, biological morphogenesis is the epitome of what can be called today a *self-organizing complex system*. To follow the metaphor proposed by Enrico Coen in his book *The Art of Genes* (Coen 1999), it could be said that the embryo is similar to a "canvas that paints itself " (where colors represent differentiated cell types) at the same time that it is growing and sculpting itself —both patterning and shaping affecting each other in a tight feedback loop.

Schematically, it means that the *mechanical* properties of cells, such as their division rate, adhesion strength, or intrinsic motility, are closely correlated with their current spatial location and temporal state of *genetic* and molecular dynamics, such as concentrations of internal

[1] available at http://mecagen.org.

proteins and external ligands, and affect each other concurrently. The genetic dynamics forms distinct *morphogenetic fields* (an emergent "hidden geography" on the embryo (Coen 1999)), while the mechanical dynamics causes these fields to expand, fold, and deform. The mechano-genetic coupling operates at the scale of individual cells, but has consequences at multiple scales across the entire embryo and throughout the whole developmental process. It creates a cascade of (non-self-similar) "fractal" re-patterning and re-shaping of the morphogenetic fields, which, as they are expanding, segment themselves again into subfields by further spatial rearrangements and differentiation of cells.

In this introductory part, we propose a brief historical summary of developmental biology, born from classical embryology (Section 1.1), followed by a review of a few important families of embryogenetic models, such as reaction-diffusion, morphogen gradients, cell shaping, and differential adhesion (Section 1.2). Then, we identify the common modeling challenges and principles that will constitute the basis of our generic model and platform, called MecaGen (Section 1.3). Its purpose is to contribute to the understanding of the coupled mechanical-genetic dynamics that drives the growth of a multicellular organism, through agent-based modeling and computational experiments.

1.1 Developmental biology

Biological development, also referred to as "embryogenesis" in the earlier stages, can be generally defined as a dynamical process leading a given organism to a certain morphological state. In that sense, studying development means investigating the mechanisms that preside over the coordination of cellular differentiation in an organism through space and time. The dynamics of morphogenesis, or "morphodynamics," is far from steady, however, as embryos often alternate phases of drastic transformations with uniform periods dedicated to growth only. The most dramatic events occur in the beginning, when the egg divides into a great number of cells within a short time. These cells soon begin to perform a collective ballet of complex movements precisely coordinated by a complex web of physico-chemical interactions. It is interesting to note that this process never ends, the morphology of an organism undergoing constant change, albeit at smaller levels of detail, until senescence and death.

The definition of development has its own embryogenesis: it has also changed and reformed itself through the numerous discoveries and practical methods that have punctuated the history of the field. Four major periods are conventionally distinguished (Hopwood 2008): (a) pre-1880: classical descriptive embryology, (b) 1880–1930: classical experimental embryology; (c) 1930–1960: reconciling genetics and embryology, leading to developmental genetics; (d) 1960-today: modern developmental biology, molecular genetics, and biomechanics.

Descriptive and experimental embryology: According to the old theory of *preformation*, organisms were believed to simply unfold and expand from miniature versions of themselves, but not create new structures. In the 1820s, Christian Pander explained that development was actually based on the transformation of primitive sheets of tissue, called the *germ layers*. During the first half of the 19th century, under the influence of Johannes Müller, the *cell theory* attempted to unify the development of various observed eggs. Cells had then become the fundamental

building blocks of every living species in the minds of the scientists. Additionally, Robert Remak stated that every cell was produced by a preexisting cell, and introduced the concept of *germ-layer specificity* in vertebrates, i.e. the fact that each layer (endoderm, mesoderm, and ectoderm) specified the type or *fate* of the cells originating from it (e.g. intestine, muscle, or skin cells).
In the 1880s, with the discipline of *Entwicklungsmechanik* (developmental mechanics), Wilhem Roux and others applied to embryos various kinds of perturbations (mechanical, thermal, chemical, or electrical) to study their effects. The key question was whether the differentiation of embryo parts was endogenous, calling it *autonomous*, or whether it was under external influence, i.e. *dependent*. Later, it was recognized that this debate had no definitive answer and reality was somewhere in the middle. Neither totally mosaic nor totally regulative, developmental principles strike a balance between both principles (Lawrence and Levine 2006). The early 20th-century embryologists refined these questions with new experiments such as grafts, in particular on the newt embryo, aimed at deciphering what determined cell fates. Ross Harrison introduced the concept of *morphogenetic fields*, then Hans Spemann and Hilde Mangold observed that a piece of tissue, the blastopore lip, when transplanted from the gastrula to another embryo, *induced* a neurulating process and the formation of a secondary embryonic axis. They called this tissue the primary embryonic *organizer*.

Developmental genetics: During the rise of genetics, Conrad Hal Waddington stressed the importance of genes in development as "controllers" of cellular fate. By comparing mutated *Drosophila* embryos, he observed that a presumptive tissue (the imaginal disc) could transform into either a leg or an antenna. He illustrated his view by the concepts of *epigenetic landscape* and *canalization*, which he compared to grooves and bumps guiding a rolling "ball" symbolizing cell fate on a hilly terrain. We will use these Waddingtonian operational concepts when coupling the mechanic and genetic parts of our model in Part 4. Developmental genetics established a new methodology for the study of embryology. Instead of perturbing tissues, *mutant* phenotypes were generated by modifying their genetic expression, especially by "knocking out" genes one by one and inferring their role in absentia. Such experiments were most systematically conducted during the 1980s by Christiane Nüsslein-Volhard and Eric Wieschaus in *Drosophila* (Nüsslein-Volhard and Wieschaus 1980) and several other model organisms, more recently in the zebrafish (Nüsslein-Volhard 2012).

Molecular genetics: The discovery of the operon-lactose mechanism by Jacob and Monod in 1961 marked the start of the molecular genetic trend in embryology. It applied the idea of induction at the subcellular level by introducing genetic determinants, the *regulator* and *operator genes*, which explain how the rate of protein synthesis was controlled by the action of *repressors*. This crucial discovery reconciled the embryological orchestration of cell behavior with the molecular paradigm. The modern view systematized the role of genetic regulators by casting them into arrays of target sites for *transcription factors* (TFs) on the DNA (Arnone and Davidson 1997). Taken together, these arrays define a web of genetic interactions called a *gene regulatory network* (GRN), whose dynamics depends on the network topology and the various TF quantities. Since 2002 rapid progress in systematic sequencing and functional genetics has led to the publication of large-scale GRN maps, such as the one underlying the early patterning of the zebrafish embryo (Chan et al. 2009). GRN dynamics is initialized by various *maternal factors* (Pelegri 2003), which are TFs already present in the egg and whose anisotropic distribution is also an important cause of the patterning of the body plan (Gavis and Lehmann

1992). Critically, it also involves communication capabilities through secretion, diffusion, and binding of extracellular ligands, which trigger transduction processes and subsequent modification of the cytoplasmic dynamics. More recently, a growing number of *epigenetic* regulatory mechanisms have also been identified, such as mechanotransduction, methylation, and other epigenetic modifications, notably "gene silencing" by RNA interference.

Cell biomechanics: Today, the post-genomic era is bringing back the cell as the integrator of the molecular and genetic machinery. Understanding precisely how the cell *behaves physically* has become a major question. Cell motility, cell adhesion, and membrane deformation are all part of the *biomechanics* underlying morphogenetic processes and their emergent features at a macroscopic level. As reviewed by Keller (2012), this field remained quiet for a long period but was recently revived. Keller distinguishes two notions in the physical shaping of embryos, already envisioned by Johannes Holtfreter in the 1930s: *selective affinity* modulated by adhesion, and *physical integration* of multiple local cellular behaviors. In particular, Holtfreter observed that cells from different germ layers mixed together were still able to recognize their lineage origins and adopt different preferential association or "affinities" accordingly. In the 1960s, Malcom Steinberg refined this idea into the *Differential Adhesion Hypothesis* (DAH) (Steinberg 1962), stating that cells are both cohesive and mutually motile in such a way that the interfacial surface tension leads the ensemble toward the most stable configuration. These concepts form the basis of more recent quantitative approaches of cell biomechanics in culture and *in vivo* (von Dassow and Davidson 2011).

1.2 Models of embryonic development

Although the works cited above made important theoretical hypotheses and proposed key ideas to explain development, they did not propose formal models *per se*, whether of a mathematical-analytical or a computational type, i.e. they performed no symbolic or numerical processing. In recent years, however, an ever increasing number of theoretical and quantitative models and simulations of development have emerged. In this section, we provide a small sampler of studies that constitute typical illustrations of the most common modeling and simulation paradigms currently in practice.

Reaction-diffusion systems: A historical landmark in the advent of developmental models was established by Alan Turing in 1952 with his work on "The chemical basis of morphogenesis" (Turing 1952). He proved that ordered patterns, such as stripes and spots of alternating color, could spontaneously arise from the amplification of unstable fluctuations in an initially homogeneous substrate. This idea was further elaborated and popularized by Gierer and Meinhardt in the 1970s (Gierer and Meinhardt 1972). They showed that, by combining "a short-range positive feedback with a long-range negative feedback," they could generate all possible Turing patterns. Typically, a pigmented medium such as an animal coat could undergo spontaneous symmetry-breaking by diffusion and reaction of an activator substance with an inhibitor substance, called *morphogens*, characterized by two different decay rates and distances (Meinhardt and Gierer 1974). This was also demonstrated by abstract models of vertebrate skin patterning, such as the stripes of the angelfish, implemented in cellular automata (Young 1984; Kondo and Miura 2010).

However, this did not imply that the *in vivo* mechanisms were actually understood. Although reaction-diffusion models can theoretically account for all sorts of patterns, biological striping phenomena where this framework applies are much more rare. For example, it is now established that the gene expression patterns in the *Drosophila* segmentation cannot be explained by reaction-diffusion models (Bieler et al. 2011). The zebrafish pigmentation offers another contrasting example of pattern that does not form via reaction-diffusion *stricto sensu*, i.e. based on putative molecules diffusing at long range, but rather via a "combination of other signaling mechanisms that have long and short functional distances" (Inaba et al. 2012).

Morphogen gradients and positional information: Most biological systems distinguish themselves by strong morphological features, i.e. an elaborate shape and body plan *architecture*, which are much more sophisticated than texture-like pattern formation. The precisely arranged body shape of animals, made of articulated segments and subparts, is not the result of free-forming random instabilities, but rather a "genomically guided" morphogenesis process. This aspect can be better captured through the paradigm of *positional information* (PI) introduced by Lewis Wolpert in the 1960s (Wolpert 1969, 2011). At an abstract level, the key idea is simply that cells must establish long-range communication system that allows them to create different parts of the organism in different locations. It is inevitable that some form of PI should be at work in multicellular organism development, embodied in various ways, for example via passive diffusion of morphogens spreading throughout the tissue or cell-to-cell intermediate-messenger signaling (Lawrence 2001; Lander et al. 2002; Tabata and Takei 2004).

Several experimental techniques have been developed to study these modes of morphogen propagation (Kicheva et al. 2012). In any case, they all give rise to concentration *gradients*, either in the extracellular matrix (ECM) or in the cells' cytoplasm. In effect, PI is a genuine *coordinate system* that self-organizes by decentralized chemical signaling among cells. Recurring at multiple levels of details in a (non-self-similar) fractal fashion, it constitutes the basis of an entire "hidden geography" covering the embryo, following Enrico Coen's image (Coen 1999), and is also employed in abstract models of development and artificial life systems (Eggenberger 1997; Kumar and Bentley 2003; Doursat 2006). On the other hand, a major issue with concentration gradients is their robustness (Barkai and Shilo 2009). Since gradient diffusion and signal propagation are highly noisy and approximative, the stability of the emergent structures is believed to rather emerge from a combination of PI *and* gene regulation, in particular via some "attractor dynamics" in the GRN (Kauffman 1969; Reinitz and Sharp 1995), amidst the continually changing spatial environment of the growing organism (Rolland-Lagan et al. 2012).

Epithelial cell shaping and division patterns: A relatively recent interest in epithelial tissue modeling has generated a certain number of models focused on cell shaping, distribution of neighborhood sizes, and division axis fields. In (Gibson et al. 2006), the authors use a Markov chain model to explain the evolution of the distribution of cell shape in the *Drosophila* epithelium. They propose that cell proliferation, not cell packing, is responsible for the shaping of cells in monolayered epithelia. The model is generalized and compared to different organisms. Other investigators (Farhadifar et al. 2007) contend that physical forces, in addition to cell division, are also required to explain epithelial cell shape in the wing disc of *Drosophila*. They use a vertex-based model in which vertices represent intersections between the junctions linking wing cells. Forces are derived from an energy function that takes into account

cell elasticity, cortical tension, and intercellular adhesion. The model is tested on experimental data obtained by laser ablation.

Sandersius et al. (2011) have investigated epithelium patterning before and during the primitive streak formation in the chick embryo. For them, against Gibson et al. (2006), non-spatial Markov models are not sufficient to explain the histogram of number of neighbors in proliferating-only epithelium. They argue that any attempt to improve biological plausibility of this type of model (e.g. with 3-sided cells or asynchronous division) induces a deviation from, instead of a refinement of, the "standard" histogram observed in various species. On the other hand, they show that their own geometrical epithelium model (based on a "Subcellular Element Model," Section 2.1) predicts the histogram with growth rate being the unique meaningful parameter.

Differential adhesion and cell sorting: The concept of patterning and compartment formation through cell sorting by differential adhesion, which was developed by Steinberg under the name of *Differential Adhesion Hypothesis* (DAH), is both powerful from a theoretical point of view and for its adequacy to describe the biological systems in agreement with typical biological observations at the tissular, cellular, and molecular level. Theoretical modeling and computer simulation in 2D and 3D of DAH-based cell sorting have been repeatedly carried out. In 1992, Graner and Glazier published their seminal cellular Potts model (Graner and Glazier 1992; Glazier and Graner 1993). Other theoretical frameworks were used to simulate similar processes: Broadland and Chen favored a finite element model (Brodland and Chen 2000), Landsberg et al. developed a vertex model for a network of adherens junctions to simulate the formation of compartments in *Drosophila* embryogenesis (Landsberg et al. 2009; Aliee et al. 2012), Beatrici and Brunnet explored the possibility to achieve cell sorting solely by motility differences in a model of self-propelled particles (Beatrici and Brunnet 2011).

The relevance of DAH has been reinforced by the characterization of cell adhesion molecules and their quantitative contribution to the surface tension in aggregates, thus providing a molecular basis to cell sorting (Foty and Steinberg 2005). The nature of the dependency between the surface tension of an aggregate and the cadherin expression level has also been explored theoretically (Zhang et al. 2011). More recent studies have tried to experimentally distinguish the respective contribution of cell adhesion and cortex tension in cell-cell contact formation, cell sorting, and tissue segregation. Heisenberg, Paluch, and colleagues approached these issues in zebrafish early development and the segregation of embryonic progenitors (Maitre et al. 2012).

1.3 Toward common modeling principles

Most of the models reviewed in the previous section were focused on specific aspects of development, whether certain episodes of embryogenesis localized in space and time, or particular mechanical or genetic components of the dynamics. The ambition of the MecaGen project is to integrate all these dimensions into one comprehensive, or *in toto*, framework.

In biological systems, three levels of organization are generally considered: the subcellular level (in which the individual elements are molecules), the cellular level (cells), and the organism level (tissues and organs). Even though cell-cell mechanical and chemical interactions are ultimately grounded in the same physics of molecular interactions (covalent, ionic, hydrogen, and electrostatic bonds), they seem to obey their own laws and "cell behavior

ontology" on a higher phenomenological level. Therefore, designing a model of multicellular development requires identifying custom laws at each level—as the reductionist dream of a huge atom-based simulation is not conceivable or just completely impractical. This involves a mix of continuous and discrete approaches, bringing analytical, statistical, and agent-based computational models together. Several works have ventured proposing such integrated frameworks at various degrees of completion and with different emphasis: multiscale mechanical forces (Blanchard and Adams 2011; van Leeuwen et al. 2009), multiscale pattern formation (Grima 2008; Little and Wieschaus 2011), multimodel and simulation platforms such as CompuCell3D (Izaguirre et al. 2004; Cickovski et al. 2007; Swat et al. 2008), or multiscale abstract models and artificial life systems (Doursat 2008; Joachimczak and Wróbel 2008; Schramm et al. 2011; Doursat et al. 2012).

The two major groups of mesoscopic properties that appear in most of these studies, and constitute the foundation of our own model, are (a) biomechanical properties and (b) genetic regulation and molecular signaling properties. The key toward understanding the morphogenesis and systemic properties of the organism lies in the *coupling* of both. It concerns how (b) influences (a) through the production and modulation of the cytoskeleton, molecular motors, and cell adhesion, but also how (a) influences (b) through the transduction of mechanical stress. The modeling work should identify the appropriate level of schematization, i.e. capture the essential causal relationships without going into fine molecular details.

Typical systemic properties of living organisms, such as development, autopoiesis or homeostasis, can only be understood through a *complex systems* approach of their underlying biological processes. Complex systems are composed of a great number of small elements that interact locally and produce a collective behavior in a decentralized and self-organized fashion. Concerning embryogenesis, this perspective requires new experimental methods, in particular the use of animal models chosen for their accessibility, transparency, and phylogenetic position. The originality of MecaGen is to directly confront the level of the complexity of living processes, something that biology has so far partly evaded in its traditional attempts to address the "function" of single genes, or dissect subcellular processes in isolated cultured cells. Now that the pieces of the puzzle have been (more or less) well identified, it is time to try and *integrate* them all together at the level of thousands of genes and millions of cells in order to see the big picture of the growing organism.

In the remainder of this chapter, the two modules, MECA and GEN, are explained separately, then coupled in Parts 2–4 (Figure 16.7 for a preview of the main components of the model and their relationships). The resulting agent-based simulations create an "in silico" embryo, i.e. a virtual test object that can be manipulated and measured in ways impossible with a real embryo. Next, Part 5 shows two illustrations on artificial data: gene regulation motifs and cell sorting, and Part 6 demonstrates a custom application of MecaGen to a real biological case study: the zebrafish early development. We take as an example the intercalation patterns appearing during the first phase of epiboly and the movements of the deep cells. Measures from the simulated embryo are confronted to measures extracted from microscopy imaging. The goal is to show that the parameters of our model can be tuned to validate the simulations, hence draw biologically meaningful conclusions. Finally, Part 7 offers a critical discussion of the choices made and perspectives for future work.

2 MECA: MODEL OF CELL BIOMECHANICS

In this first part of the model, we formalize the mechanical interactions and behavioral properties of the cells. We begin with a brief review of various biomechanical models (Section 2.1), in continuous or discrete spaces, of geometrical or physical nature, paying closer attention to *off-lattice, particle-based methods*, which will be the basis of our own approach. Next, we present a *discrete-element model using one particle per cell*, driven by an overdamped equation of motion (Section 2.2) of the type $\lambda\vec{v}_i = \vec{F}_i^P + \vec{F}_i^A$, where $\vec{v}_i$ is the velocity of one cell i, $\vec{F}_i^P$ represents "passive" interaction forces controlling cell stiffness and adhesion (Section 2.3), and $\vec{F}_i^A$ represents "active" interaction forces, i.e. specific cell behavior, such as protrusive activity or apical constriction, based on polarization axes. (Section 2.4). These forces are calculated by adding contributions from cells j in the neighborhood $\mathcal{N}_i$ of cell i, defined by topological criteria.

2.1 Challenges in biomechanical modeling

Through his theory, Wilhelm Roux established the importance of mechanics in the study of developmental systems. Since then, a great number of theoretical models of biomechanics have been proposed at various levels of abstraction—and speculation. Depending on the researchers' background and their focus of interest, embryogenesis has been assimilated to differential geometry, pattern formation, fluid dynamics, material physics, systems architecture, cellular automata or collective motion, among many disciplines. In particular, the growth and shaping of cells, tissues and organs have been variously compared to manifolds, balloons, tensegrity structures, bubbles, swarms, and so on. This diversity is due to the extremely elusive nature of multicellular systems compared to the traditional objects studied by classical mechanics. Whereas the Newtonian framework is well suited to fixed objects presenting high spatiotemporal regularities, living matter is riddled with heterogeneity, irregularities, and ceaseless internal adaptivity. Local cell behaviors and global tissue properties can change rapidly as they rest upon a molecular structure in constant flux and state of self-reorganization. Therefore, this heterogeneity of behaviors gave rise to a heterogeneity of models, unfortunately not always compatible with each other. Nonetheless, these attempts are useful to help capture pieces of the puzzle and bring us closer to a more accurate and complete rendition of organism development.

We distinguish here between "macroscopic" models relying on continuous space and "microscopic" models relying on discrete elements. The latter will constitute the basis for the *particle-based* approach that we follow in our own model.

Macroscopic viewpoint: continuous-space laws: Macroscopic descriptions of the embryo set behavioral laws directly at the global tissular level without explicit underlying cellular or molecular components. They are generally based on macroscopic partial (spatial) differential equations, which have the benefit of compactness, as they offer an inclusive representation of development in one or a few formulas. On the other hand, the main disadvantage of grand formalisms is often too much generality or vagueness, with a consequent lack of operational tools. In any case, cell tissue in this paradigm is construed as a continuous mass, equivalent to an infinity of infinitesimal points. Mathematical biology (Murray 2003) epitomizes the continuum

mechanics paradigm, which is broadly divided into *solid mechanics* and *fluid mechanics* approaches. A distinctive feature of solids and fluids is their unequal ability to resist the action of a tangential shearing force. Both fields distinguish different types of bulk behavior and both have been applied to biological matter and multicellular tissue. In the case of fluids, stresses are linked to velocity fields through a continuity equation and conservation laws. In the case of solids, stresses are linked to a deformation tensor (strain) (Fleury 2005).

Microscopic viewpoint: discrete-element rules: Microscopic descriptions of biological tissue consider the cells that constitute it (sometimes the subcellular structures and molecules, too) as autonomously acting components. It is their collective behavior that determines the mechanical properties of the tissue at the emergent level. As the elements of discrete models do not always coincide one-to-one with cells (being possibly subcellular or supracellular), they are alternatively called "particles." Their properties generally include spatial coordinates and geometric features, and optionally mechanical and physical properties. There are four main groups of discrete models, depending on whether particles are confined to a discrete grid or not, and whether cells are made of several particles or only one: (i) on-lattice models with one particle per cell, corresponding to *cellular automata* (extensively reviewed by Deutsch and Dormann (2005)); (ii) on-lattice models with multiple particles per cell, essentially represented by the *Cellular Potts Model* (introduced by Graner and Glazier (1992) and best exemplified by Marée and Hogeweg (2001)); (iii) off-lattice models with one particle per cell, composed of a 2D/3D irregular network whose vertices represent cells and edges represent cell-cell interactions (typically as in the *Delaunay-Object-Dynamics* model by Schaller and Meyer-Hermann (2004)); and (iv) off-lattice models with multiple particles per cell, in which the fine grain of subcellular particles is preserved (most notably the *Subcellular Element Model* (ScEM) of Newman (2005)). The framework we eventually adopted in MecaGen belongs to category (iii) and its specific features are explained below.

2.2 Central equation of cell motion

The biomechanical model presented here is a type of *particle-based physics*, meaning that cells are represented by "particles"—here, only one per cell. The classical Newtonian *equation of motion* describing a particle with mass m and acceleration $\vec{a}$ reads $m\vec{a} = \vec{F}(\vec{X}, \vec{v}, R)$, where the sum of forces $\vec{F}$ can depend on the particle's location $\vec{X}$, velocity $\vec{v}$, and/or radius R. Cells, however, are small, ambivalent fluid-solid entities, and their interactions are "sticky," which makes their inertial forces negligible with respect to viscosity (corresponding to a low Reynolds number). In that case, applied forces become proportional to velocity, not acceleration: if $m \ll \lambda$, then $m\vec{a} = -\lambda\vec{v} + \vec{F}$ yields $\lambda\vec{v} = \vec{F}$.

Generalizing to a multicellular swarm S, the motion of each cell i is governed by the sum of forces $\vec{F}_{ij}$ exerted by all other cells j belonging to its neighborhood $\mathcal{N}_i$:

$$\lambda_i \vec{v}_i = \sum_{j \in \mathcal{N}_i} \vec{F}_{ij} = \sum_{j \in \mathcal{N}_i} \vec{F}^P_{ij} + \vec{F}^A_{ij} = \vec{F}^P_i + \vec{F}^A_i \tag{16.1}$$

where $\vec{F}^P_i$ represents "passive" interaction forces, $\vec{F}^A_i$ represents "active" interaction forces (explained in Sections 2.3 and 2.4), and the damping coefficient is proportional to the surface

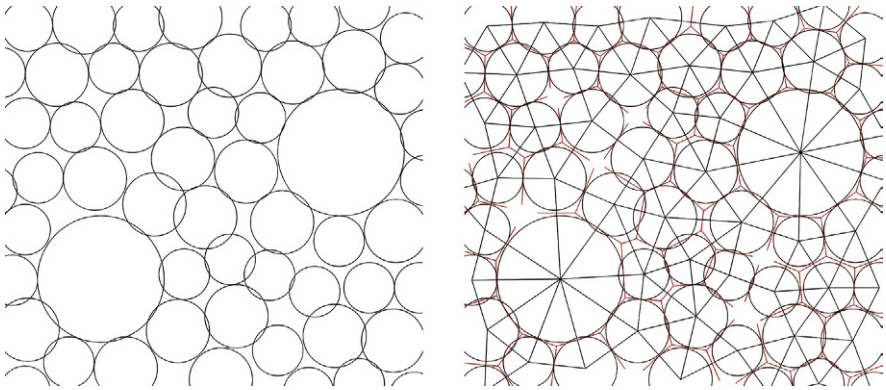

FIGURE 16.1 Output of the neighborhood algorithm. Left: A 2D swarm of cells characterized by various given positions and radii. Right: The neighborhood links (black edges, radiating from the centers) and contact areas (red edges, tangential to the circles) between cells calculated by the method described in this section. (For interpretation of the references to color in this figure legend, the reader is referred to the web version of this book.)

area of the cell: $\lambda_i = \lambda_0 {R_i}^2$. The neighborhood $\mathcal{N}_i$ is calculated in two steps: first, a preselection of potential neighbors that obey certain *metric* criteria, then a refinement of this list according to *topological* features (Figure 16.1). According to the metric criteria, two cells of radius R_i, R_j and locations $\vec{X}_i, \vec{X}_j$ are considered neighbors if their distance is smaller than a cutoff value:

$$\mathcal{N}_i^m = \left\{ j \in S : \left\| \vec{X}_i - \vec{X}_j \right\| \leq c_{\max}(R_i + R_j) \right\}. \tag{16.2}$$

In the following, we denote $r_{ij} = \left\| \vec{X}_i - \vec{X}_j \right\|$ and $r_{ij}^{\max} = c_{\max}(R_i + R_j)$, i.e. $r_{ij} \leq r_{ij}^{\max}$ for neighbor cells i and j. Although cells are "spheroidal," they also have the possibility to deform in order to interact with farther away neighbor cells. Radius $r_{ij}^{\max}$ sets the maximum distance of this deformation. To evaluate $c_{\max}$, we established an empirical law relating r_{ij} to the contact area between i and j, denoted by A_{ij}, such that it vanishes for $r_{ij} = r_{ij}^{\max}$:

$$A_{ij} = A(r_{ij}, R_i, R_j) = a(r_{ij} - r_{ij}^{\max})^2 \text{ iff } r_{ij} < r_{ij}^{\max}, \quad \text{otherwise } 0. \tag{16.3}$$

In the absence of real data, we constructed an artificial testbed experiment to infer an approximate relationship. It consisted of an ellipsoidal domain that was filled with three consecutive generations of dividing cells, then distorted in various ways to force the cells into different spatial rearrangements. We found the best empirical fit for values $a = 1.3697$ and $c_{\max} = 1.2414$, which are used throughout the model.

A purely metric neighborhood, however, is not viable as it often leads to collapsing volumes during simulation when adhesion between interacting cells is high. This is why we ultimately used a topological neighborhood denoted by $\mathcal{N}_i^t$, based on a variant of the Voronoi diagram and its dual, the Delaunay triangulation, called a *Gabriel graph*. In 2D, this method imposes that no node be found inside the circle whose diameter is a valid neighborhood edge. We generalized the Gabriel criterion to the 3D case using spheres as follows:

$$\mathcal{N}_i^t = \left\{ j \in \mathcal{N}_i^m : \forall k \in \mathcal{N}_i^m, \quad \left\| \vec{X}_k - \frac{1}{2}(\vec{X}_i + \vec{X}_j) \right\| \geq \frac{r_{ij}}{2} \right\}. \tag{16.4}$$

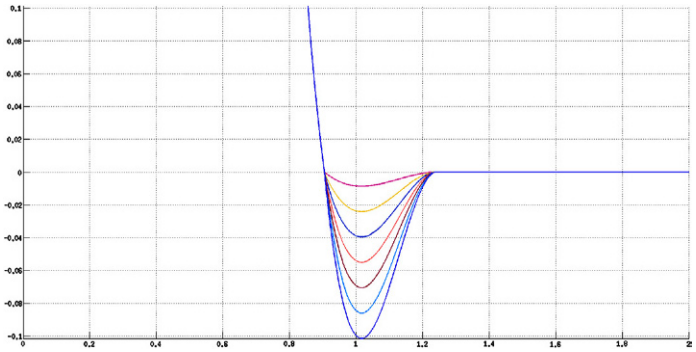

FIGURE 16.2 Plot of the interaction potential E^P with distance, under various values of the adhesion coefficient w_{adh}. The relaxation force $\vec{F}^P$ is derived from E^P. Curves are composed of three domains: repulsion at short range (until the minimum, i.e. $F = 0$), attraction at mid-range (after the minimum), and neutrality at long range (constant F). See text for details.

2.3 Interaction potential forces

For every pair of neighboring particles (i, j) we focus in this section on the interaction potential E_{ij}^P from which the "passive, or *relaxation*" force $\vec{F}_{ij}^P$ is derived. Like most particle-based interaction potential models, we distinguish three distance domains (Figure 16.2): (a) a *repulsion* domain (decreasing E) at distances shorter than an equilibrium distance defined by $r_{ij}^{eq} = c_i^{eq} R_i + c_j^{eq} R_j$, where c_i^{eq} is a coefficient that may depend on the cell; (b) an *attraction* domain (increasing E) at distances greater than r_{ij}^{eq}; and (c) a *neutral* domain (constant E) beyond the maximum limit of the interaction field $r_{ij}^{max} = c_{max}(R_i + R_j)$.

Toward short distances, as soon as two cells touch each other, adhesive forces tend to increase their contact area A_{ij} until inner resistance compensates the push. This implicitly defines an equilibrium surface area and distance. Accordingly, the expression of the relaxation force is made of three parts:

$$\vec{F}_{ij}^P = \begin{cases} -A_{ij} w_{rep}(r_{ij} - r_{ij}^{eq}).\vec{u}_{ij} & \text{if } r_{ij} < r_{ij}^{eq} \\ -A_{ij} w_{adh}(r_{ij} - r_{ij}^{eq}).\vec{u}_{ij} & \text{if } r_{ij} \geq r_{ij}^{eq} \text{ and } r_{ij} < r_{ij}^{max} \\ \vec{0} & \text{if } r_{ij} \geq r_{ij}^{max} \end{cases} \tag{16.5}$$

where $A_{ij} = a(r_{ij} - r_{ij}^{max})^2$ is the contact area introduced earlier, while the depth of the well is controlled by a repulsion coefficient w_{rep} until r_{ij}^{eq} and an adhesion coefficient w_{adh} beyond r_{ij}^{eq}.

In the previous section, we estimated a universal average value for coefficient c_{max} based on empirical statistics of the contact areas between neighboring particles. Here, we need to estimate the equilibrium coefficients c_i^{eq} of the relaxation forces. For this, we rely on the densest arrangement of sphere packing, in which each sphere touches 12 other spheres, as an approximation. In this scenario, we obtain a uniform value $c_i^{eq} \equiv c_{eq} = (\pi/(3\sqrt{2}))^{1/3} \simeq 0.904$.

2.4 Behavioral forces

Another crucial difference with solid objects is that surrounding cells are responsible not only for dampening motion but also for motion itself. To progress, a cell needs to cling and push back surrounding cells, somewhat like a swimmer pushes back water to move forward. Thus, in addition to the passive attraction/repulsion forces $\vec{F}_{ij}^{P}$, we introduce *proactive behavioral* forces $\vec{F}_{ij}^{A}$, composed of an "intrinsic" term $\vec{F}_{ij}^{A,\text{int}}$ and its "extrinsic" counterpart $\vec{F}_{ij}^{A,\text{ext}}$, whose purpose is to provide a schematic model of the cells' specialized biomechanics. During development and across numerous species, cells manifest a wide variety of mechanical properties and behavioral phenomena. We focus here on one such mechanism, *cellular protrusion*, which we believe is the main driving force in the zebrafish early gastrulation.

2.4.1 Protrusion behavior

Cell protrusion is essentially a *cyclic* activity, similar to the activity of tracked vehicles (such as tanks) except that, since inertia plays no part in cellular interactions, adhesion is regulated in a special way to avoid sliding between the cell surfaces in contact. Protrusive activity induces an *intercalation* of the cell between its neighbors. One condition is the presence of an *axis of polarization*, which is generally related to the diffusion of external ligand molecules and an asymmetrical distribution of internal substances (explained in Part 4). This axis can also be caused by mechanotransduction from neighboring cell-cell contacts, or feedback from the active forces themselves, but these aspects are not modeled here. In any case, it determines two regions of the cell, or *poles*, where protrusive activity occurs: if only one pole is active, the cell is called "monopolar"; if both are active, it is called "bipolar."

At the subcellular level, the main structure underlying protrusion is the cellular scaffolding of the *cytoskeleton*, whose three main components are microfilaments (similar to an "envelope" that contracts and dilates), intermediate filaments ("cables" exerting a tension), and microtubules ("beams" resisting compression). To explain protrusion, we focus on the microfilaments, which constitute most of the cell cortex, a mesh-like network made of actin and myosin molecules that lie just below the plasma membrane and are attached to it by catenin molecules. The active deformation of this acto-myosin network, essentially by (re)polymerization of actin, provides the driving mechanism of protrusion (Figure 16.3).

The coupled action of acto-myosin cortex and the focal adhesion points form a sort of "treadmill" originating at the tip of the protrusion (Figure 16.4). This movement induces a torque transmission between the protruding cell and each of the neighbor cells attached by focal adhesion points. The transfer of cell material in the bulge results from the "intrinsic" force generated by the acto-myosin cortex, while the "extrinsic" force is exerted on the adjacent cell through the focal adhesion points. In some cases, an additional mechanism of cellular contraction at the back of the cell (not included here) amplifies the intrinsic force. We assume that the distribution of focal adhesion points is homogeneous on the surface area of the cell, so the quantity of torque transmitted between two neighboring cells i and j is proportional to their contact area A_{ij}.

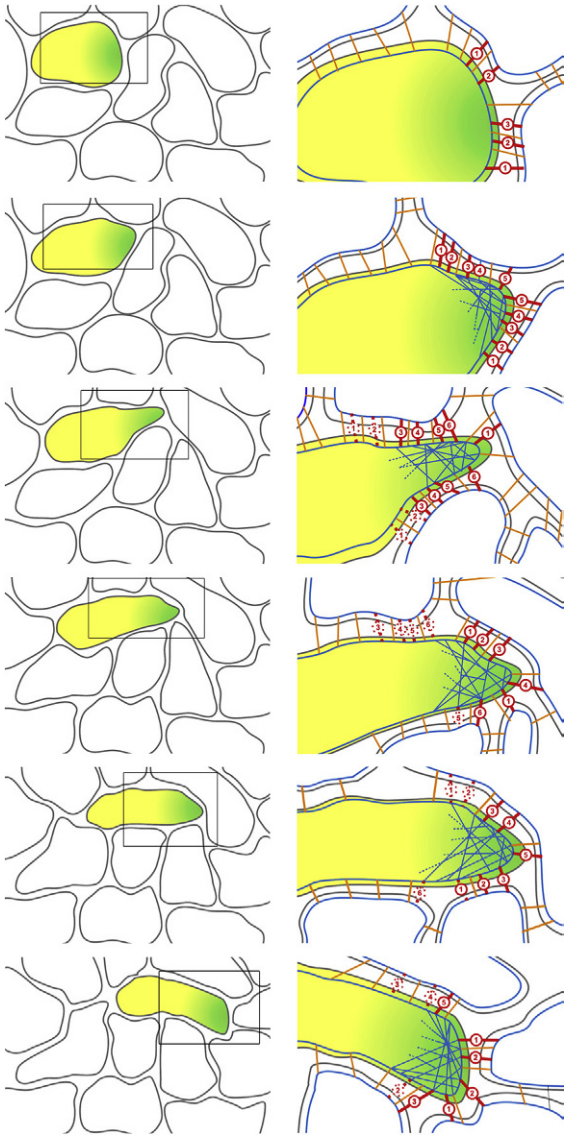

FIGURE 16.3 Cellular protrusion illustrated at the subcellular level. A cell is attached to its neighbors by molecular bridges (essentially cadherin molecules, symbolized by thin orange edges), which actively deform their internal acto-myosin cortical network in the direction of the polarization axis (blue mesh of lines and curves) indicated by the internal chemical gradient (yellow-green shades across the cell). A bulge eventually appears at the active pole, pushing away neighboring cells. No intercalation process would be observed, however, without a precise regulation of the adhesion contacts between the cells. Thus, in addition to the regular adhesion bonds, special *focal adhesion points* (thick red edges carrying numbers) also appear at the surface of the protruding region of the cell. These bonds bear extra load generated by the protrusive activity of the acto-myosin cortex. They become visible around the tip of the bulge and, as the cell is advancing, maintain spatial cohesion between neighboring cytoskeletons. Without them, the cell would slip on the surface and the efficiency of the protrusion would be greatly reduced. Focal adhesion points gradually disappear from the cell membrane as the cell advances relatively to the bonded neighbors. (For interpretation of the references to color in this figure legend, the reader is referred to the web version of this book.)

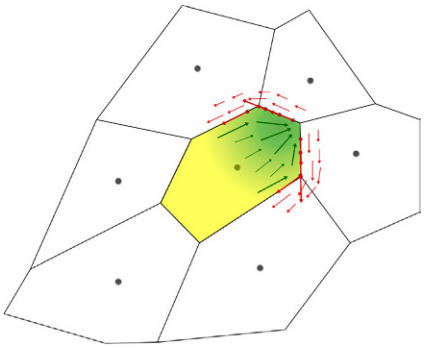

FIGURE 16.4 Idealized view of the protrusive activity in MECA. Internal arrows represent the cell interior flow and external arrows the cell neighborhood flow, as the central cell exerts a protrusion over its surroundings. The schematized focal adhesion points of Figure 16.3, which appear at the tip of the cell, move back then disappear as the cell moves forward.

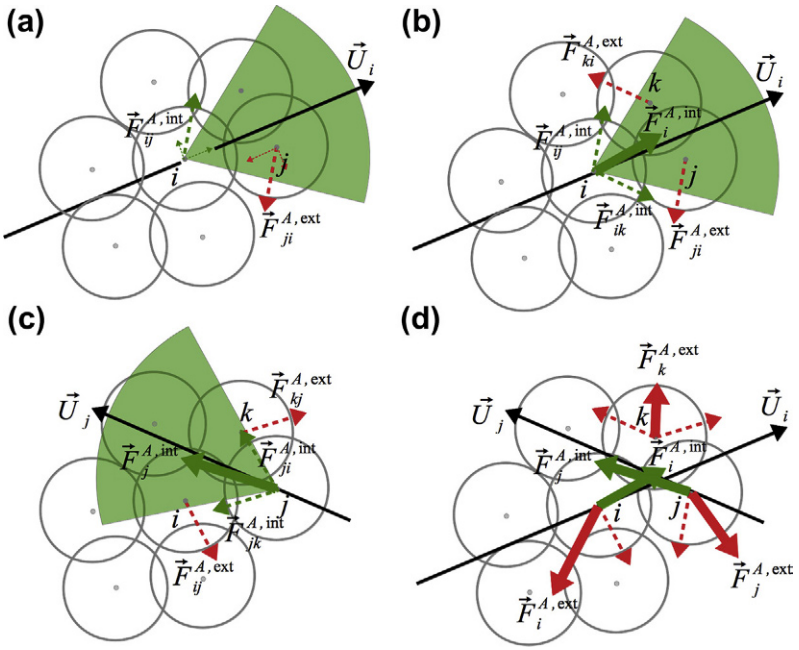

FIGURE 16.5 Schematic representation of active protrusive forces in MECA. See text for details. These schemas illustrate the formalization of the idealized mechanism of Figure 16.4 in the particle-based framework. (a, b) The polar domain (green slice) of cell i, denoted by $\mathcal{N}_i^{t+}$, contains two neighbor cells j and k, over which i exerts a protrusive force. "Intrinsic" forces are shown in green and extrinsic forces in red. (a) Highlighting one pair of opposite forces. (b) Forces produced by i's activity. (c) Forces produced by j's activity if j, too, happens to be protruding. (d) The net resulting "active" forces (not shown) are obtained by adding the net resulting "int" (thick green) and "ext" (thick red) arrows on each cell. (For interpretation of the references to color in this figure legend, the reader is referred to the web version of this book.)

2.4.2 *Active force model*

In our particle-based framework, the mathematical interpretation and representation of this mechanism is the following (Figure 16.5a): a cell i possesses a normalized *polarization axis* $\vec{U}_i$ (black arrow), considered given in this part. Inside $\mathcal{N}_i^t$, we denote by $\mathcal{N}_i^{t+}$ the sublist of neighbors that make contact with cell i on its "positive" pole, i.e. are positioned relative to i in the same general direction as $\vec{U}_i$ (green pie-slice domain, covering two cells j and k in the figure):

$$\mathcal{N}_i^{t+} = \left\{ j \in \mathcal{N}_i^t : \frac{\vec{X}_j - \vec{X}_i}{\left\| \vec{X}_j - \vec{X}_i \right\|} \cdot \vec{U}_i \geq \eta \right\} \tag{16.6}$$

A threshold value η controls the relative size of the protrusion (the opening of the pie slice). Similarly, we denote by $\mathcal{N}_i^{t-}$ the sublist of neighbors that share a contact area on the "negative" pole of the cell, i.e. away from the polarization vector. This opposite neighborhood is used in the case of an opposite monopolar or a bipolar protrusion behavior.

In the regular monopolar case illustrated here, for each neighbor $j \in \mathcal{N}_i^{t+}$, a pair of equal and opposite forces contribute to the motion of both i and j: an intrinsic force $\vec{F}_{ij}^{A,\text{int}}$ (larger dashed green arrow in Figure 16.5a) and its simultaneous and exact counterpart $\vec{F}_{ji}^{A,\text{ext}}$ (larger dashed red arrow), such that $\vec{F}_{ji}^{A,\text{ext}} = -\vec{F}_{ij}^{A,\text{int}}$. The common axis of these forces is designed to roughly emulate the profile of the contact area that can be seen in the polygonal representation of Figure 16.4 (but not in the disc-particle representation of Figure 16.5). It is a linear combination of the unitary protrusion axis $\vec{U}_i$ and its orthogonal complement $\vec{U}_i^{\perp j}$ passing through j:

$$\vec{F}_{ij}^{A,\text{int}} = f^A A_{ij} . \left(\cos(\nu)\, \vec{U}_i + \sin(\nu)\, \vec{U}_i^{\perp j} \right) \tag{16.7}$$

where the angle ν tunes the profile of the contact area (small dashed arrows resulting in the larger dashed arrows in Figure 16.5a) and coefficient f^A tunes the intensity of the force. The angle could be precisely calculated as a function of the angular position of each neighbor, but we deemed such sophistication unnecessary and opted instead for a constant value of $\arctan(4/3) \approx 53°$ (experiments with other values around 45° showed no significant difference).

Suppose for now that only cell i exerts a monopolar protrusive activity on its neighbors (Figure 16.5b). For each $j \in \mathcal{N}_i^{t+}$, this creates a pair of forces $\vec{F}_{ij}^{A,\text{int}}$ and $\vec{F}_{ji}^{A,\text{ext}}$ as described above. Therefore, the total behavioral force generated by i's protrusion (solid green arrow, not necessarily parallel to $\vec{U}_i$ in 3D) is the sum of its neighbors' contributions: $\vec{F}_i^{A,\text{int}} = \vec{F}_{ij}^{A,\text{int}} + \vec{F}_{ik}^{A,\text{int}}$ (dashed green arrows). Similar, if j also protrudes, then an equivalent set of forces is created around it (Figure 16.5c, symmetric of Figure 16.5b). In that case, combining both protruding activities from i and j, each cell in the neighborhood can be the site of both intrinsic and extrinsic forces (Figure 16.5d): the former come from its own protruding activity (green arrows), the latter from the protruding activity of its neighbors (red arrows). In this particular illustration, the third cell k is not protruding, thus its own total active force is only made of extrinsic components coming from i and j. The sum of "int" and "ext" forces on i (resp. j and k) yields the

net "active" force on this cell (not shown in Figure 16.5d), which corresponds to $\vec{F}_i^A$ (resp. $\vec{F}_j^A$ and $\vec{F}_k^A$) in its motion equation. Each net active force leads a cell to move alongside its neighbors and pass through.

Finally, at the scale of the whole embryo, the net global force resulting from this complex field of local intrinsic/extrinsic active forces is zero, due to their mutual compensation: $\vec{F}^A \equiv \sum_i \sum_{j \in \mathcal{N}_i} \vec{F}_{ij}^A = \sum_i \vec{F}_i^A = \vec{0}$. This is a reasonable expectation, as the relative movements of cells with respect to each other (protrusion, constriction, migration, etc.) should not have the effect of moving the embryo but only reshaping it.

Summary: The biomechanical model MECA proposes basic rules that are sufficient to simulate the physics of a high number of cells in a deforming tissue. Among its original features, we have defined a new neighborhood based on an adaptation of the Gabriel rule to 3D sets of particles; we have obtained a new approximation of the classical inter-particles force potential (of the Morse or Lennard-Jones type) by scaling an elastic potential via an estimation of the contact area; we have also distinguished "passive" interaction forces, responsible for simple attraction and repulsion, from "active" interaction forces, responsible for more complex cell behaviors such as protrusion. Altogether, these modeling choices allow us to carry out massive computational simulations and explore large domains of parameter space relatively quickly (Part 6).

3 GEN: MODEL OF GENETIC REGULATION AND MOLECULAR SIGNALING

The goal of this part is to briefly review the principles of gene regulatory networks (GRNs) and chemical signaling, and describe the corresponding components of our model. The molecular and genetic interactions occurring during development are a subject of intense research (Wilczynski and Furlong 2010; Ben-Tabou and Davidson 2009; Giacomantonio and Goodhill 2010), at the crossroads between bioinformatics, systems biology, and chemical kinetics. Nonetheless, we believe that relevant insight can already be gained by adopting three simple and easily computable types of rules: (1) a set of rules driving the dynamics of *intracellular* gene/protein reactions (Section 3.1); (2) rules driving the dynamics of cellular secretion and transduction, linking the intracellular with the extracellular milieu (Section 3.2); and (3) rules driving the dynamics of *extracellular* reactions, transport, and diffusion (Section 3.3).

These rules are generally expressed in a chemical kinetic framework by ordinary differential equations (ODEs) of the type $dp/dt = f(p, g, q, r)$, where p represents protein concentrations, g gene expression levels, q external ligands, and r membrane receptors. Extracellular reactions, transport, and diffusion of ligands are also taken into account via partial differential equations (PDEs) involving $\partial q/\partial t$ and fluxes $\vec{J} = -D\vec{\nabla}q$.

3.1 Intracellular gene and protein reactions

Protein concentrations $\mathbf{p} = \{p_a\}$ representing the various protein types P_a inside the cell can evolve through (i) protein-protein reactions, (ii) synthesis by encoding genes, or (iii) degradation by the molecular environment. Conversely, gene activities $\mathbf{g} = \{g_b\}$ are regulated by the

proteins (bypassing RNA) via Boolean functions representing a logical combination of promoters and repressors. For example, two protein reactants yielding one protein product can be formalized by the following reaction and rate equations:

$$P_0 + P_1 \xrightarrow{k} P_2 \quad \text{with} \quad \begin{cases} \dot{p}_1 = -k' p_1 + \gamma_1 g_1 - \kappa_1 \\ \dot{p}_2 = +k' p_1 + \gamma_2 g_2 - \kappa_2 \end{cases} \tag{16.8}$$

where $k' = kp_0$ is the linear "pseudo-coefficient" of the reaction, assuming that P_0 is predominant ($p_0 \gg p_1$) and its variations negligible, γ_a is a linear rate of P_a's synthesis by encoding gene G_a, and κ_a is a constant rate for P_a's degradation.

Conversely, the activity of a gene G_b can be enhanced by the presence of promoting transcription factors (TFs) and/or the absence of repressing TFs. Here, a TF is assumed to be one of the proteins P_a and we denote by $P_a \curvearrowright G_b$ its structural ability to bind one of the cis-regulatory sites of G_b (regions of DNA near the gene sequence). Since multiple TFs may simultaneously influence a single gene, a binary matrix $\mathbf{\Gamma} = \{\Gamma_{ab}\}$ is a well-suited schematization (Peter et al. 2012):

$$\Gamma_{ab}(t) = 1 \text{ iff } P_a \curvearrowright G_b \text{ and } p_a(t) \geq \theta_{ab}, \quad \text{otherwise } 0 \tag{16.9}$$

where θ_{ab} is the concentration threshold above which protein a effectively binds site b. Then, the activity of gene G_b is determined by the output of a logic function f_b, a combination of the Boolean operators AND, OR, and NOT: $g_b(t) = f_b(\mathbf{\Gamma}(t))$. For example, if f_b is a pure AND operator, then all promoters must be present and all repressors absent to activate G_b. If it is a pure OR operator, then a single promoter suffices.

3.2 Signal secretion and transduction

Cells in the developing embryo communicate chemically through various means. Two of the most common mechanisms are: (a) *secretion*, typically by exocytosis, of proteins or metabolites through the cell membrane, and (b) *transduction* via receptors in the membrane, by which a signal triggers a second messenger on the other side. The interfacing module connected to the GRN that exports and imports these molecules will be generically named here *ligands*. A ligand Q_a can be externalized from the cellular domain into the space between cells, called "interstitium," with a secretion rate σ_a. Conversely, an extracellular signal can be transduced into an intracellular protein through a *signal transduction* module, comprising a receptor protein R_{ab} on the membrane, to which Q_a can bind and trigger the intracellular synthesis of protein P_b. The corresponding kinetic equations are not detailed here.

3.3 Extracellular reactions, transport, and diffusion

Various models of the spatial configuration of the interstitium have been elaborated (Kojić et al. 2010), but we prefer using the graph of neighborhood relationships $\mathcal{N}_i$ derived from the Gabriel rule (Section 2.2) to serve as transport infrastructure. The diffusion dynamics is based on Fick's law, stating that ligands move from high- to low-concentration regions

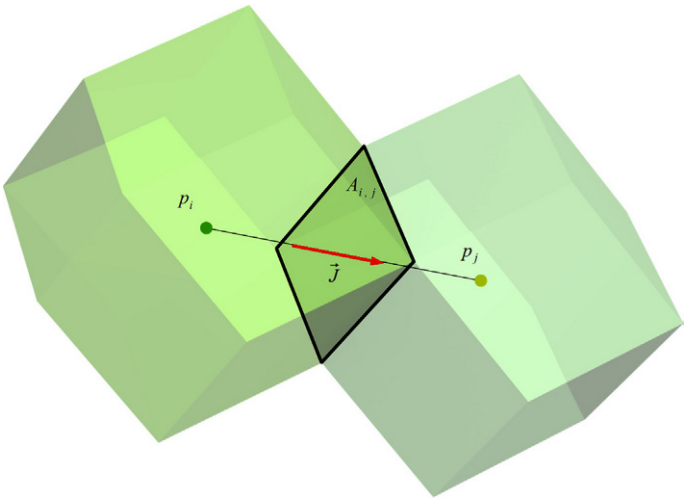

FIGURE 16.6 Schema of the flux of ligand. Here, $\vec{J}$ represents $\vec{J}_{a,ij} = \vec{J}_{a,ji}$, the flux of ligand Q_a between the cellular volumes occupied by neighboring particle-cells i and j.

proportionally to the *gradient* of concentration. Therefore, a discrete approximation of the flux of ligand Q_a on the edge between cell i and j, denoted by $\vec{J}_{a,ij}$, reads

$$\vec{J}_{a,ij} = -D_a \frac{q_{a,j} - q_{a,i}}{r_{ij}} \vec{u}_{ij} \tag{16.10}$$

where $q_{a,i}$ is the ligand's concentration near the surface of cell i, D_a a diffusion coefficient, $\vec{u}_{ij}$ the unit vector from i to j, and $r_{ij} = ||\vec{u}_{ij}||$ (Figure 16.6). Note that this expression is invariant by reversal of direction. Then, the temporal evolution of the concentration is determined by the *continuity equation*, which is a local form of conservation law. The divergence theorem gives the integral form of the continuity equation, applied to the volume of the cell. Its continuous expression is

$$\frac{\partial q_{a,i}}{\partial t} + \iint_O \vec{J}_{a,i}.\vec{dA} = s_{a,i} + d_{a,i} \tag{16.11}$$

where $\vec{J}_{a,i} = \sum_j \vec{J}_{a,ij}$ is the total flux of ligand a with respect to cell i, $\vec{dA}$ is the normal vector of the closed surface of the cell, $s_{a,i}$ is the "source" term corresponding to the rate of ligand produced by secretion, and $d_{a,i}$ is the "sink" term corresponding to the rate of extracellular ligand Q_a disappearing by transduction (terms from Section 3.2 not detailed here). Finally, importing the previous discrete approximation, we obtain

$$\frac{\partial q_{a,i}}{\partial t} = D_a \left(\sum_{j \in \mathcal{N}_i^t} \frac{A_{ij}}{r_{ij}} (q_{a,j} - q_{a,i}) \right) + s_{a,i} + d_{a,i} \tag{16.12}$$

Summary: The GEN model of genetic regulation and molecular signaling provides a new adaptation of the classical reaction-diffusion framework to a moving substrate. The

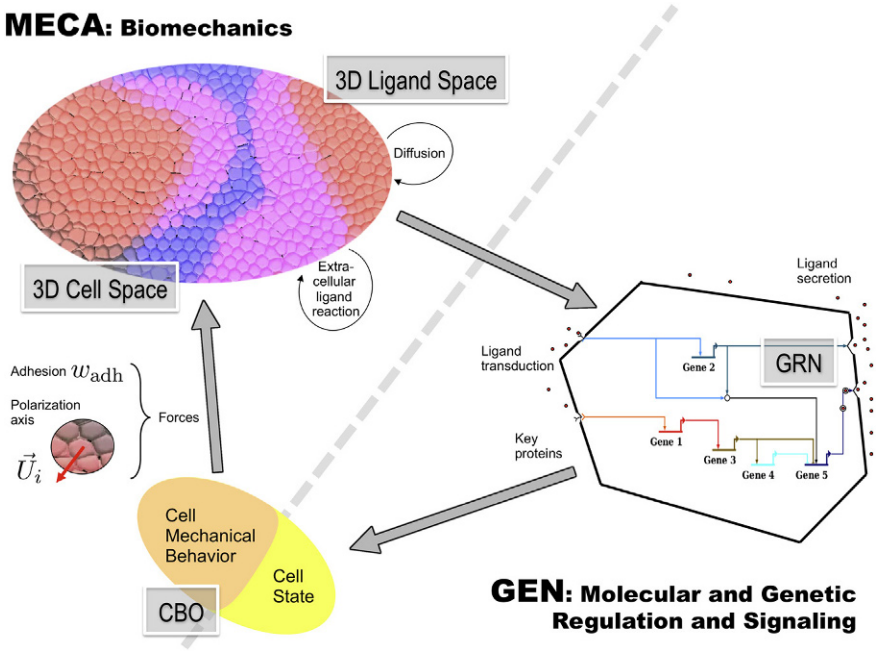

FIGURE 16.7 Flowchart of the complete MecaGen model, illustrating its core principles. Three modules are described in this chapter. (1) A particle-based framework supports both the biomechanics (3D cell space, Part 2) and the extracellular diffusion (3D ligand space, Section 3.3). (2) Intracellular molecular signaling and genetic regulation are modeled by a GRN via differential equations and Boolean operators (Section 3.1). (3) A cell behaviorontology (CBO) is also discussed in Section4.1. Here, we temporarily simplify this diagram by introducing a custom cell differentiation tool, the Waddingtonian Timeline Specification (WTS, Section 4.2), which allows us to test the other mechanisms in artificial contexts (Part 5) as well as real biological scenarios (Part 6).

discretized form of the ligand diffusion equation relates the local concentrations of ligands to the cells' positions. As a consequence, the ligand patterns can be modified by deformation of the tissue. Moreover, each cell can independently harbor chemical "reactions" organized into genetic and molecular processes that are modeled by differential equations and Boolean operators. Communication between the intracellular protein quantities and the extracellular ligand quantities is achieved by transduction and secretion modules. Similarly to the MECA part, these features allow running simulations that involve thousands of cells in reasonable computing time.

4 MECAGEN: MODEL OF MECHANIC-GENETIC COUPLING

This last part lays out the foundations of an integrated morphogenetic model linking biomechanics (from Part 2) and genetic regulation/molecular signaling (from Part 3). To this goal, it proposes a "cell behavior ontology" (CBO) relating *cell states* to *cell behaviors*. Ideally, a complete model would "plug" the MECA and GEN modules into each other via this CBO,

as illustrated in Figure 16.7. For the moment, however, we restrict ourselves to a simplified scheme bypassing the actual molecular and genetic processes on the GEN side. Kinetic equations are replaced with predefined cell states, or *cell types*, serving as entries into a "lookup table" containing one set of output values per cell type or pair of cell types. Only the diffusion dynamics of Section 3.3 is preserved here. This continuous-to-discrete abstraction has been commonly practiced (Thomas 1973) and will allow us to test the mechanical hypotheses introduced in MECA.

4.1 Cell behavior ontology

First, biological systems modeling requires the choice of an ontology, i.e. a hierarchy of predefined *categories* and relationships among them. Here, the appropriate candidates are the various cell behaviors that occur during a developmental process. In our model, we propose a simpler mapping between the dynamical rules of MECA and those of GEN. Ideally, mechanical properties should "emerge" from the regulative molecular microstructure, represented by a certain subset M of intracellular protein concentrations $\mathbf{p}_i = \{p_{a,i}\}_{a\in M}$. In particular, genetic output should determine the values of the two main mechanical parameters: the adhesion coefficient w_{adh} of the relaxation forces (Section 2.3), and the polarization axes $\vec{U}_i$ determining active protrusion (Section 2.4). In principle, such parameters are local functions of pairs of cells (i, j) via $(\mathbf{p}_i, \mathbf{p}_j)$. Instead, they depend here on pairs of *cell types*, denoted by $(\mathcal{T}, \mathcal{T}')$. For example, the adhesion coefficients become $w^{\text{adh}}_{\mathcal{T}\mathcal{T}'} = w_{\text{adh}}(\mathbf{p}_{\mathcal{T}}, \mathbf{p}_{\mathcal{T}'})$, where $\mathbf{p}_{\mathcal{T}}$ is typically an average over $\{\mathbf{p}_i\}_{i\in\mathcal{T}}$. Other features, such as cell cycle length and cell volume control, are always decoupled from genetic regulation, and receive fixed parameter values. Yet other mechanisms, such as cell death and the structure of the extracellular matrix (ECM), are not included for now.

4.2 Waddingtonian timeline specification

We "read out" behavioral parameters of the CBO directly from a new tool that we call a *Waddingtonian Timeline Specification* (WTS, Section 1.1), for which a dedicated graphical user interface was created (Figure 16.8a). The first step in setting up a WTS is to "carve the hillside" by specifying a temporal series of *cell types* $\{\mathcal{T}(i,t)\}$ that cells may adopt during the developmental process, along with the transition rules among these types. To this aim, we segment the timeline into *stages* delimited by particular points in time $\{t_1, t_2, \ldots\}$ at which new cell types may be introduced. For example, Stage 2 corresponds to the time interval $[t_2, t_3)$. During any given stage, cells may transition from one existing type to another type under the rules specified in a table (see next). The overall WTS structure can be represented by a pseudo-tree of cell types, with lateral transfers among the branches, expanding over time.

4.2.1 Differentiation table $\mathscr{D}$

To specify the conditions inducing a cell to change its type, we rely on the classical concept of *differentiation*. In our simplified model, cell differentiation depends on a Wolpertian *positional information* mechanism (Section 1.2). During stage S, corresponding to interval $[t_S, t_{S+1})$, if

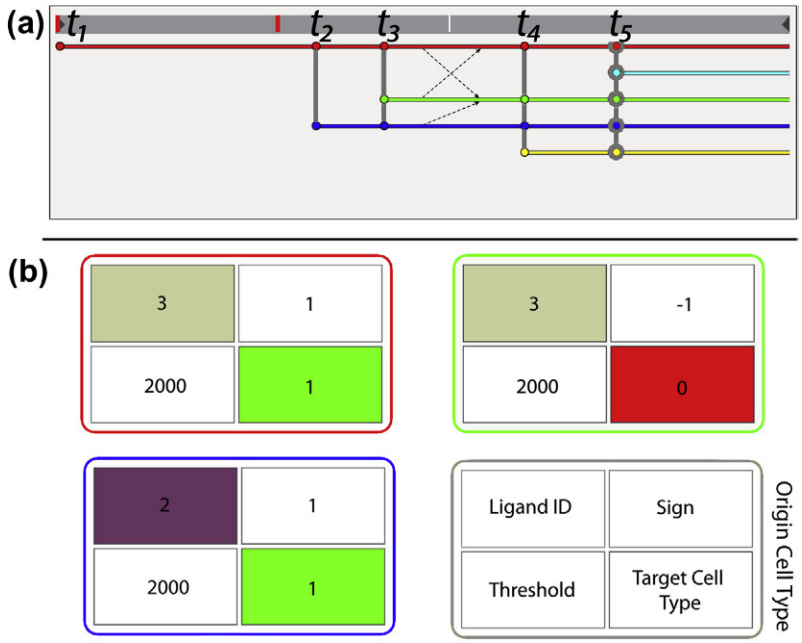

FIGURE 16.8 **Waddingtonian timeline of cell types $\{\mathcal{T}(i,t)\}$ and differentiation table $\mathscr{D}$.** (a) The gray bar at the top is the time axis (oriented left to right), segmented into stages $S = [t_S, t_{S+1})$. The colored horizontal branches symbolize the types that cells can potentially take, corresponding to the grooves of a Waddingtonian landscape. Here, five stages in the timeline indicate the onset of one type (red), two types (red and blue), …, until five types (red, cyan, green, blue, yellow). Differentiations, i.e. type transitions, may happen within each stage, for example shown here in Stage 3: the three thin dashed arrows represent the differentiation table ((b), see below), indicating that type red may become green, green may become red, and blue may become green. In this WTS graphical interface, stages can also be selected manually to specify their parameters (next figures): here, Stage 5 is selected by clicking on t_5, which is represented by gray circles on all the type nodes. (b) Differentiation table $\mathscr{D}_3$ representing the possible type transitions during Stage 3. It contains three differentiation modules displayed in one column, one module by origin type. In each module, the current cell type $\mathcal{T}(i,t)$ is represented by the round-corner frame color, the target cell type by the color (or id) of the bottom-right block, and the ligand-threshold-sign triplet $(Q_a, \theta_a, \epsilon_a)$ by the top-left block's color (or id), bottom-left block's value, and top-left block's value. Each cell changes its type depending on whether $\epsilon_a q_{a,i} \geq \epsilon_a \theta_a$. Bottom right: The generic template of one differentiation module inside one origin type, as followed by the other three modules. (For interpretation of the references to color in this figure legend, the reader is referred to the web version of this book.)

the local ligand concentration $q_{a,i}$ of molecular species Q_a on cell i crosses (i.e. either exceeds or sinks below) a given threshold θ_a, then cell i changes types. Generally, the new type is a function of the current type via a *differentiation operator* $\mathscr{D}$ represented by a ruleset or "lookup table" predefined for each stage S (Figure 16.8b), which we denote by $\mathscr{D}_S$. This table is organized in modules indexed by triplets composed of the ligand species, their differentiation thresholds, and the threshold signs. A module can be denoted by $\mathcal{T}(i,t) \leftarrow \mathscr{D}_S\big[\mathcal{T}(i,t), \{(Q_a, \theta_a, \epsilon_a)\}_{a \in M}\big]$, where the sign ϵ_a expresses whether the condition is about an exceeding or a sinking concentration, which can be written $\epsilon_a q_{a,i} \geq \epsilon_a \theta_a$.

4.2.2 *Passive adhesion table* $\mathscr{P}$

Once the differentiation backbone of the WTS has been established, the *adhesion coefficient* parameters of relaxation forces $\vec{F}_{ij}^{p}$ can be specified for each pair of cell types, thus we can denote them by $w_{TT'}^{\text{adh}}$ for $i \in \mathcal{T}$ and $j \in \mathcal{T}'$. Since passive adhesion forces are symmetrical, we have $w_{TT'}^{\text{adh}} = w_{T'T}^{\text{adh}}$ and these values can be organized into a triangular $\mathcal{T} \times \mathcal{T}'$ matrix, denoted here by $\mathscr{P}$. An example can be seen in Figure 16.11.

4.2.3 *Ligand sinks and sources table* $\mathscr{L}$

At each stage S, we define sources and sinks for each ligand through another table denoted $\mathscr{L}_S$. Each cell type can potentially secrete or absorb any ligand type Q_a. Additionally, the *spatial configuration* of the ligand sources must also be specified. The module used for this type of specification can be seen in the example of Figures 16.11 and 16.16. We define, per cell type, the id of the ligand and the geometrical border of the volume of secretion. Assuming a spherical embryo, an orthonormal coordinate frame is set up along the animal-vegetal (AV) axis, antero-posterior (AP) axis, and bilateral symmetry left-right (LR) axis. On each axis, we define two cutoff values to extract a slice, then take the intersection of all three slices to define the source region of ligand release. Several such source regions can be defined per cell type. Thus the spatial ligand source table is composed of sextuplets of cutoff coordinate values for each ligand inside each cell type module. External sources of ligands, such as the yolk (see example in Figure 16.16), may also be added.

4.2.4 *Active protrusion table* $\mathscr{A}$

Finally, once the ligand sources/sinks table $\mathscr{L}$ is defined, the "active" cell behavior can be set up by adding other behavioral modules for a given cell type at a given stage. To this aim, we define an active protrusion table $\mathscr{A}$ composed of modules associated to an origin cell type, whose parameters are explained below. Every "active" cell behavior exploited in MecaGen requires a *polarization axis*. In real cells, polarization correlates with an asymmetry of intracellular molecular concentrations. In our model, since we adopted one particle per cell, there can be no spatialization of intracellular material. Thus we chose to represent this asymmetry by 3D vectors $\vec{U}_i$ passing through the centers of the cells (Section 2.4). More precisely, a cell i can be potentially polarized by multiple mechanisms as the developmental process unfolds, corresponding to multiple "candidate" polarization axes. These modes of polarization determination can be: (a) a local gradient-based or "chemotactic" mode (one of the possible GEN-to-MECA coupling links), (b) a cell-cell contact propagation mode or (c) a force-induced mode (both of the MECA-to-MECA sort), and (d) a default mode used only if a polarized cell has no input to trigger any of the above three mechanisms, in which case the axis is randomly reoriented until another polarization mode takes over.

When a new polarization axis $\vec{U}_i'$ has been calculated via one of these four modes, the current axis is updated through an inertia coefficient ω according to $\vec{U}_i \leftarrow \omega\,\vec{U}_i + \vec{U}_i'$, followed by renormalization to keep the vectors unitary. In the remainder of this chapter, we only use the chemotactic mode (a) to modulate the dynamics of protrusion with ligand diffusion (beside the default mode (d), which is only a random reset). The hypothesis underlying mode (a) is that a cell is able to detect an asymmetry of extracellular ligand concentration in its local

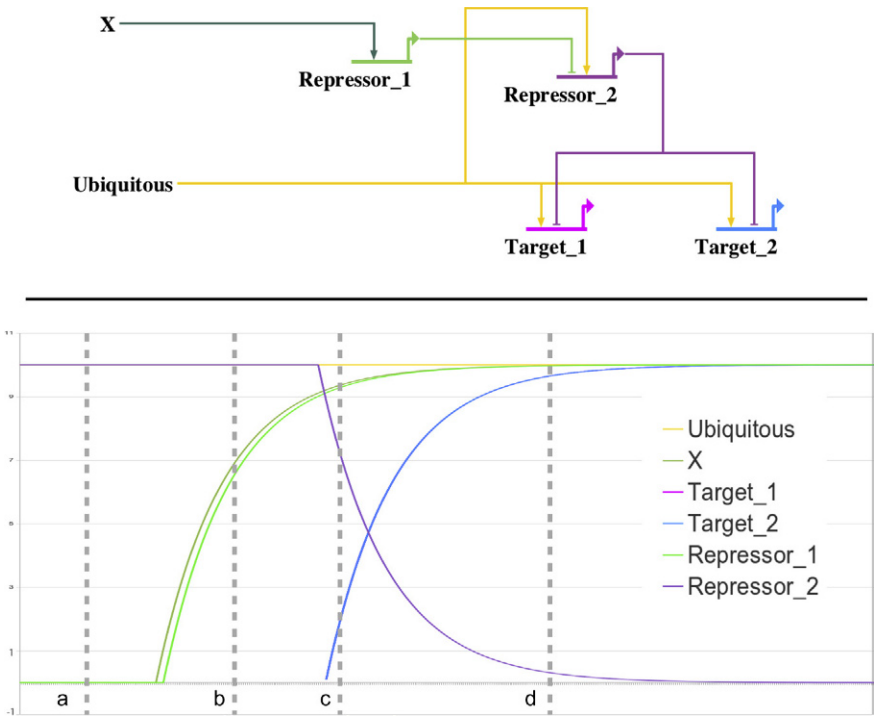

FIGURE 16.9 "Double negative gate" GRN subcircuit and protein concentration dynamics. Top: Network map. Bottom: Evolution of protein concentrations in the region where X is expressed. See text for the explanation of the curves' profile. The tagged vertical bars a, b, c, and d indicate the timing of the snapshots shown in Figure 16.10. The curve of Target1 (pink) is hidden by the curve of Target2 (blue) as their dynamics is exactly the same. (For interpretation of the references to color in this figure legend, the reader is referred to the web version of this book.)

vicinity. Accordingly, the candidate axis of polarization is calculated by a linear average of the neighborhood edges $\vec{u}_{ij}$, in which the weights are functions of the differences in ligand concentrations:

$$\vec{U}_i' = \sum_{j \in \mathcal{N}_i^t} (q_{a,j} - q_{a,i})^m \vec{u}_{ij} \tag{16.13}$$

where $q_{a,i}$ is the local quantity of extracellular ligand Q_a surrounding i (Section 3.3), and m is an integer controlling the sensibility of detection of local concentration differences (m must be odd to conserve vector directions, typically $m = 3$).

Putting these features together, each module of the active protrusion table $\mathscr{A}$ is composed of four parameters (see example in Figures 16.11 and 16.16):

- the target cell type $\mathcal{T}'$ that the protrusion is affecting,
- the chosen index among all the various candidate axes of protrusion $\{\vec{U}_i\}$, which can be calculated here only by one of the ligand-based mode (a) or random mode (d),

- the intensity f^A of the protrusive force (Section 2.4; the length of the dashed arrows in Figure 16.5),
- a ternary value equal to $+1$ if the cell is monopolar in the direction of $\mathcal{N}_i^{t+}$, -1 if it is monopolar in the opposite direction $\mathcal{N}_i^{t-}$, or 0 if it is bipolar i.e. protruding in both directions.

Summary: The Waddingtonian timeline concludes our modeling framework. It is a novel, yet limited, method of specifying cell behaviors through space and time. It allows a partial exploitation of the principles involved in MecaGen but is sufficient to start exploring the mechanical space and coupling principles. We now illustrate this framework on artificial data (Part 5), then on a biological case study of intercalation patterns in the zebrafish early development (Part 6).

5 ILLUSTRATIONS ON ARTIFICIAL DATA

5.1 Gene regulation motifs

This section offers a glimpse of the possibilities of our genetic regulation and molecular signaling model through a simple, idealized example. We follow here Eric Davidson's article "Emerging properties of animal gene regulatory networks" (Davidson 2010), which describes various small GRN subcircuits, showing their involvement in embryonic development, and focus on one of them: the *double negative gate*. Our example is a small part of the sea urchin embryo's GRN (Peter and Davidson 2009; Davidson 2009) allowing the activation of a series of genes in a specific region of the embryo under the control of localized expression, represented by protein X (Figures 16.9, 16.10). The interesting feature of this circuit is that X does not directly promote the set of regulated genes (Target1 and Target2), but rather *inhibits inhibitors* of these genes (Repressor1 and Repressor2). The net effect is that the target genes are expressed in a particular region of the embryo and shut down everywhere else.

We illustrate the dynamics of this particular motif in an artificial cell population comprising 4,886 cells laid out in a thin 3D space delimited by two planes at a distance equivalent to two cell diameters (Figure 16.10). The cells are assumed immobile, in a mechanical equilibrium state, and no active forces are present.

- In the beginning, protein Ubiquitous (present in all cells) activates at the same time genes Target1 and Target2 *and* their repressor Repressor2, so that only the protein encoded by Repressor2 is expressed ubiquitously (Figures 16.9a and 16.10a).
- At a later point in time, protein X is introduced in one region of the cell population by switching its concentration rate in these cells to a constant value of 0.1 unit per time step. In parallel, all proteins have a similar degradation rate of 0.99 unit per time step, so that the concentration of X tends toward an equilibrium quantity of 10 units.
- As soon as the concentration of X exceeds a binding threshold $\theta_{\text{X,Rep1}} = 1$ on the cis-regulatory element of Repressor1, the corresponding protein is produced at a rate of 0.1 unit per time step. (Figures 16.9b and 16.10b).
- Once the concentration of protein Repressor1 exceeds in turn another threshold $\theta_{\text{Rep1,Rep2}} = 9$, the Repressor2 gene state is switched to 0 via the AND Boolean function relating the Repressor1 and Ubiquitous transcription factors.

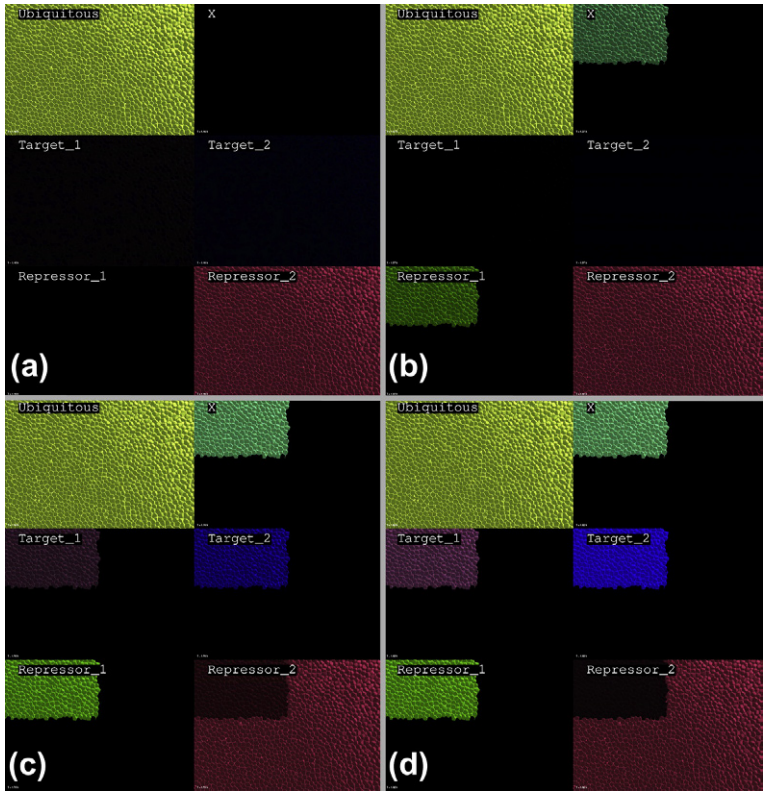

FIGURE 16.10 Spatial evolution of protein concentrations in the double negative gate experiment. The letters correspond to the bars of Figure 16.9. Each image is composed of six simultaneous views of the simulated cell population. View location (correlated with color) represents the protein type, from left to right and top to bottom: Ubiquitous, X, Target1, Target2, Repressor1, Repressor2. Shade represents the protein concentration (dark for low, bright for high). The top left corner of each image is the region where protein X is artificially secreted.

- Finally, the concentration of Repressor2 protein, which is no longer produced by its encoding gene, decreases by degradation. Once it passes below concentration thresholds $\theta_{\text{Rep2,Tar1}} = \theta_{\text{Rep2,Tar2}} = 9$ on the sites of genes Target1 and Target2 via another AND operator, the target genes start to be expressed in the spatial region of the X protein (Figures 16.9c and 16.10c).

The temporal evolution of all proteins is shown in Figure 16.9, and their spatial map in Figure 16.10.

5.2 Cell sorting

A main point of MecaGen is that a cell's motility is due to its protrusive activity. In this section, we illustrate this principle through an abstract simulation of *cell sorting*. Historically, spontaneous cell rearrangement is one of the multicellular phenomena most studied by

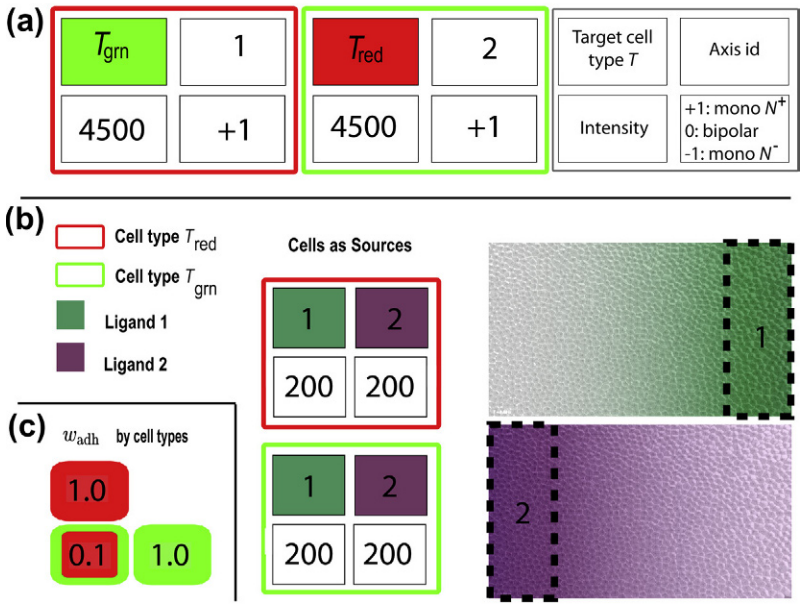

FIGURE 16.11 Tables for the cell sorting experiment. See definition in Section 4.2 and text for details. (a) Active protrusion table $\mathscr{A}$: protrusion behavior here is heterotypic, i.e. cells act only upon neighboring cells of a different type. Axis id 1 (resp. 2) is the gradient-based polarization mode (a) with ligand 1 (resp. 2). (b) Ligand diffusion table $\mathscr{L}$: both cell types secrete both ligand types Q_1 and Q_2 with the same rates $s_1 = s_2 = 200$, in simulation units. They do this, however, only if they enter one of the source regions on either vertical border of the domain. (c) Passive adhesion table $\mathscr{P}$.

theoretical models, notably the Differential Adhesion Hypothesis (DAH) (Steinberg 1962) and the Cellular Potts Model (Graner and Glazier 1992) (Section 1.2). These models often use a "temperature" parameter, derived by analogy from thermodynamics and corresponding to an intrinsic cell motility coefficient (Zhang et al. 2011), which controls membrane fluctuations and sorting efficiency. We perform here a similar experiment, but explore our own parameter ontology based on the orientation of the polarization axis. We start from the same cell tissue as Section 5.1 with the essential difference that cells can now move but not change types. In the WTS framework presented above, it means that we are zooming inside one stage S with only two horizontal cell type lines, one red and one green, and no transition arrows between them, i.e. no differentiation table $\mathscr{D}$. Initially, cells are randomly assigned one of two cell types: a "red" cell type $\mathcal{T}_{\text{red}}$ and a "green" cell type $\mathcal{T}_{\text{grn}}$, creating two populations of fixed size.

Passive adhesion table $\mathscr{P}$: Taking after the DAH, we postulate that both cell populations have a *strong homotypic adhesion*, i.e. a large adhesion coefficient w_{adh} for the passive forces exerted between cells of the same type, and a *weak heterotypic adhesion*, i.e. a small adhesion coefficient between cells of different type. Using our previous notations from Section 4.2, this results in a simple two-type table $\mathscr{P}$ (Figure 16.11c) with one high value $w^{\text{adh}}_{\mathcal{T}\mathcal{T}} = w^{\text{adh}}_{\mathcal{T}'\mathcal{T}'} = 1.0$ and one low value $w^{\text{adh}}_{\mathcal{T}\mathcal{T}'} = w^{\text{adh}}_{\mathcal{T}'\mathcal{T}} = 0.1$, where $\mathcal{T}, \mathcal{T}'$ stand for $\mathcal{T}_{\text{red}}, \mathcal{T}_{\text{grn}}$.

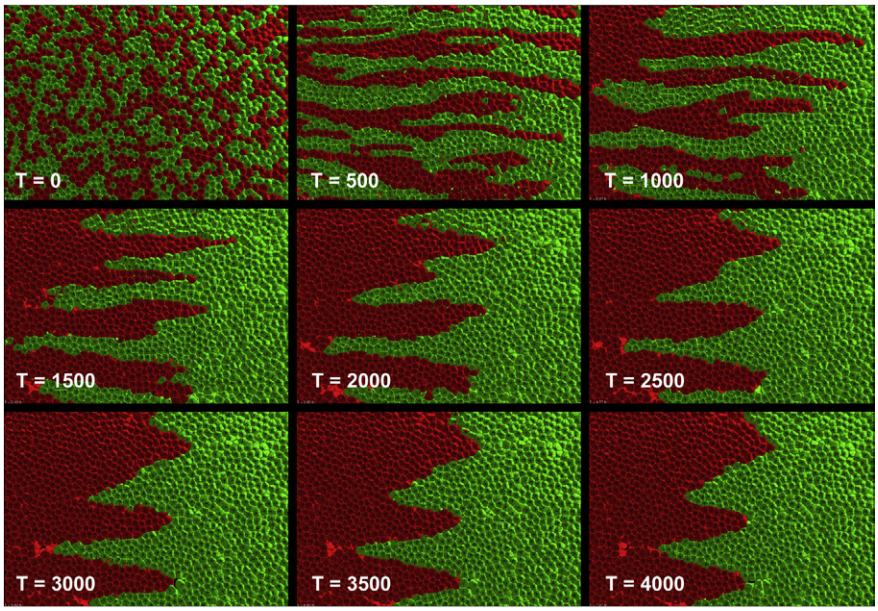

FIGURE 16.12 Ligand-based heterotypic protrusion, planar diffusion sources. See text for comments. Two hidden ligands are diffusing from the left and right borders of the cell bilayer. Green (right-half) cells' polarization axes are oriented toward the right source and red (left-half) cells' axes toward the left source. Each cell type is exerting monopolar protrusion over the other cell type (heterotypic contacts).

Ligand table $\mathscr{L}$: Polarization axes are specified by the ligand-based chemotactic mode (a) (Section 4.2). Two different ligand molecular species are secreted, Q_1 and Q_2, and both types of cells $\mathcal{T}_{\text{red}}$ and $\mathcal{T}_{\text{grn}}$ are potential sources for these ligands with the same secretion rates s_1 and s_2 (Figure 16.11b). No cell absorbs any ligand, so there is no boundary condition on the low concentration end. On the high concentration end, however, there is a spatial constraint on where the ligand sources are located: two rectangular domains are predefined on the left and right border of the frame, and whenever a cell of any type enters the right (resp. left) domain, it starts secreting Q_1 (resp. Q_2).

Active protrusion table $\mathscr{A}$: In this particular experiment, the protrusive behavior is heterotypic, i.e. red cells protrude on the green cells only, and vice versa. It means that the active mechanical interactions described in Figure 16.5 occur at the interface between the two populations, not within populations. Another rule is that $\mathcal{T}_{\text{red}}$ cells respond only to the gradient created by ligand Q_1, and $\mathcal{T}_{\text{grn}}$ cells only to Q_2. The rest of the active protrusion table $\mathcal{A}$ (Figure 16.11a) concerns the protrusion force intensity f^A and the polarity, which is +1 here for both cell types, meaning that all cells protrude in the uphill direction of their preferred gradient. The net effect is that red cells orient their polarization axis toward the left border (higher q_1 concentration values) and green cells toward the right border (higher q_2).

Results: Although cells collectively exhibit a clear sorting behavior (Figure 16.12), we observe that the boundary line between the two populations does not become flat, as

would be expected from a classical DAH study. In the present experiment, all cell polarization axes $\vec{U}_i$ are roughly colinear and aligned with the horizontal direction. This is because at later stages (here, after time step 3500), the profile of the boundary line between the red and green populations is directly related to η, the dot-product limit determining the "positive" polar neighborhood $\mathcal{N}_i^{i+}$ centered around $\vec{U}_i$ (Section 2.4; pie slice in Figure 16.5). Due to this limit, a green cell near the boundary line, which protrudes toward the right side of the tissue, does not have any more red cells in its polar neighborhood, therefore the equilibrium state of tissue dynamics displays a jagged boundary line. In conclusion, the manner in which protrusion behavior is modeled here is not sufficient to obtain the smoother boundary of regular cell sorting phenomena, and would require additional mechanisms.

6 BIOLOGICAL CASE STUDY: INTERCALATION PATTERNS IN THE ZEBRAFISH EPIBOLY

The zebrafish early development is the site of multiple morphogenetic events that illustrate the links between microscopic cell behaviors and macroscopic deformations. We choose to examine more closely and treat one of these events by modeling and simulation in order to illustrate the applicability of the MecaGen framework to biological data.

6.1 Hypotheses and model

We focus here on the first phase of a major developmental event, the *epiboly*, occurring between 3.3 hours postfertilization (hpf) and 5.5 hpf. It is characterized by a flattening of the deep cell mass and its spreading over the yolk cell toward the vegetal pole (Figure 16.13). At 3.3 hpf, or "high stage," the deep cells lie on top of the yolk, sandwiched between the yolk syncytial layer (YSL) and a population of newly differentiated epithelial cells, called the enveloping layer (EVL). The interface between YSL and EVL is called the "margin." As flattening occurs, the deep cells start to *intercalate radially*, i.e. migrate from the depth of the blastoderm toward its surface. The qualitative description highlighted by the names of the developmental stages, "high," "oblong," and "sphere," refers to the flattening of the blastoderm and suggests that the overall shape of the embryo becomes gradually closer to spherical. Then, at 5.3 hpf, i.e. about 50% of the epiboly stage, the yolk bulges inside the blastoderm, forming a dome shape until the depth of the blastoderm is uniform over all latitudes.

While intrinsic deep cell behaviors are supposed to be responsible for most of the deformation of the embryo at these stages, we cannot exclude an active participation of the YSL or the newly differentiated EVL to the epiboly. In the present case study, we use two kinds of measures: macroscopic measures characterizing the doming phenomenon, and microscopic measures characterizing the intercalation patterns, in order to show that the intrinsic behavior of deep cells is sufficient to trigger upward yolk bulging (doming motion) and downward margin progression toward the yolk's equatorial latitude. In this context, we also evaluate how the YSL margin and the EVL's tangential stiffness modulate the deep cells' driving force.

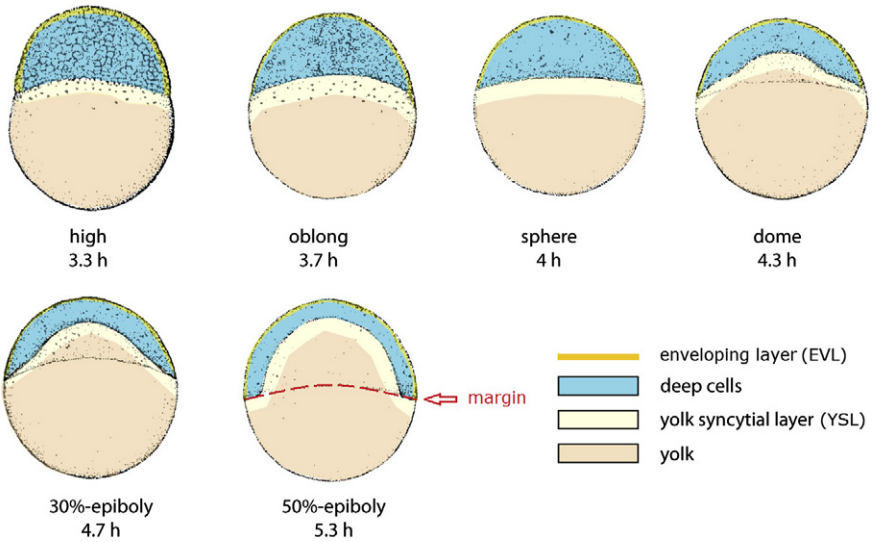

FIGURE 16.13 **Zebrafish early gastrula stages.** Adapted from Kimmel et al. (1995), with permission. From the high stage to the 50% epiboly stage: lateral views with animal pole to the top and dorsal side, identified by the shield stage, to the right. The enveloping layer (EVL) is in yellow, the yolk syncytial layer (YSL) in pale yellow, and deep cells in blue. The whole spatio-temporal sequence is expected to last 2 h at 28.5 ° C. (For interpretation of the references to color in this figure legend, the reader is referred to the web version of this book.)

6.1.1 Passive margin sliding scenario

We envision five possible, but non-exclusive scenarios explaining how the margin moves toward the vegetal pole (Figure 16.14): (i) the internal YSL (iYSL) actively spreads over the yolk (in its cortical region), carrying both the deep cells and the EVL margin with it; (ii) the EVL actively spreads over the blastoderm, carrying the margin with it; (iii) the margin is pulled downward by an active mechanism in the external YSL (eYSL); (iv) some active mechanism inside the yolk triggers the convex bulge inside the blastoderm area; and (v) the deep cells actively intercalate and their collective behavior induces a pressure at the marginal region, pushing the resisting margin toward the vegetal pole.

Scenarios (i) and (iii) would require some active mechanism in the network of microtubules linking the yolk syncytial nuclei (YSN), either by pushing from the iYSL or pulling from the vegetal eYSL. Disruption of the microtubules with nocodazole at the sphere stage is not sufficient, however, to stop the epibolic motion (Solnica-Krezel and Driever 1994). Scenario (ii) would require an active flattening of the EVL apico-basal thickness and conjugated extension of its lateral surface. It would imply that, at the margin, the EVL would move toward the yolk equatorial latitude ahead of the deep cells, but this is not what we observe in our imaging data (Figure 16.14). The inside of the yolk has also not been described to contain a well-structured cytoskeleton. This penalizes the possibility envisioned by scenario (iv) of an active mechanism occurring in this domain.

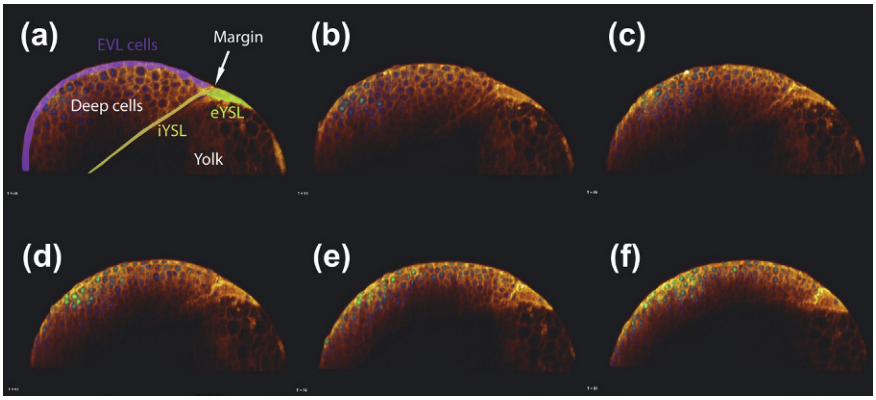

FIGURE 16.14 Wild type zebrafish embryo imaged live from the oblong stage to 30% epiboly. We observe here a slice passing approximately through the center and the animal pole of the embryo. a: oblong stage. b: transition between oblong and sphere stage. c: sphere stage. d: transition between sphere and dome stage. e: dome stage. f: transition from dome to 30% epiboly stage (dataset 071222bF from Nadine Peyriéras's lab).

All the experiments described in the literature indicate that epiboly is a robust process, probably relying on several redundant mechanisms. However, since the only scenario that has not been contradicted in the literature is (v), our goal will be to show by modeling and simulation in MecaGen that active intercalation of the deep cells is sufficient to drive epiboly during the studied period. This particular scenario requires *a mechanism that will convert the push exerted by the deep cells over the margin into a sliding movement of the margin toward the vegetal pole*. We describe here how this mechanism is modeled.

6.1.2 MECA: force model

The marginal deep cells are stuck in the corner formed by the YSL and the EVL. We expect that the margin will slide toward the vegetal pole if the norm of the tangential force exerted by the deep cells (DC) on the marginal yolk membrane particles (MYM), denoted by $\vec{F}_{ij}^{\text{m:D},\parallel}$, is larger than a given "resistance threshold" $\theta_{\text{m},\parallel}$ (Figure 16.15c). We call this force the "pushing force" as it expresses the localized quantity of force exerted by a DC particle j over an MYM particle i. Its equation reads:

$$\vec{F}_{ij}^{\text{m:D},\parallel} = \begin{cases} -w_{\text{rep}}^{\text{ym:D}}(r_{ij}^{\parallel} - r_{ij}^{\text{eq},\parallel}).A_{ij}(r_{ij}^{\parallel}, R_i, R_{\text{ym}}).\vec{U}_{\text{ym},i}^{\parallel} & \text{if } r_{ij}^{\parallel} < r_{ij}^{\text{eq},\parallel} \\ \vec{0} & \text{if } r_{ij}^{\parallel} \geq r_{ij}^{\text{eq},\parallel} \end{cases} \tag{16.14}$$

where the repulsion coefficient $w_{\text{rep}}^{\text{ym:D}}$ is the same as the one controlling the repulsion at the YM-DC interface, A_{ij} is the contact area, $r_{ij}^{\parallel}$ is the dot product of the relative position vector $r_{ij}\vec{u}_{ij}$ and the tangential vector $-\vec{U}_{\text{ym},i}^{\parallel}$ of the MYM particle i (Figure 16.15c,d), and $r_{ij}^{\text{eq},\parallel} = c_{\text{eq}}(R_i + R_{\text{ym}})$. Only the repulsive part of the force ($r < r^{\text{eq}}$) has a non-zero formulation because we do not consider here the reverse situation of marginal deep cells going back toward the animal pole of the yolk and pulling the margin with them.

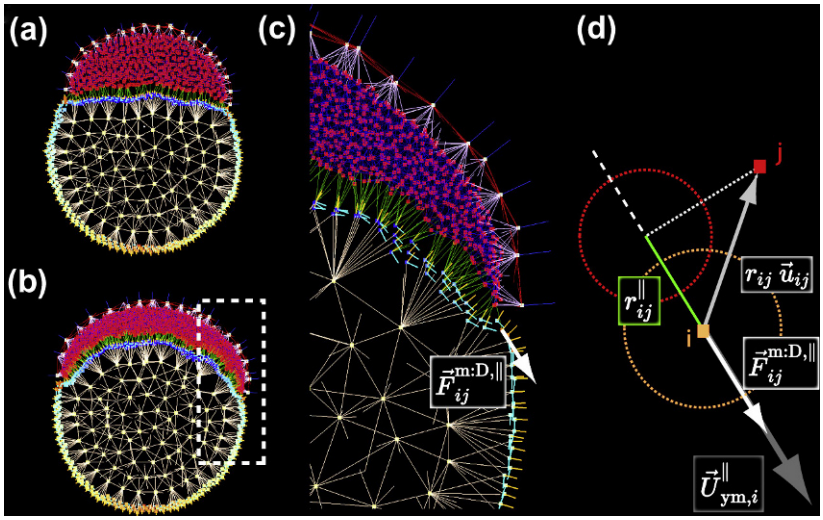

FIGURE 16.15 Mechanism controlling the passive sliding of the blastoderm and EVL margin toward the vegetal pole. a: Sagittal section of the simulated embryo at the onset of epiboly. b: Sagittal section at 30% epiboly. c: Zoom on the marginal region of the embryo at 30% epiboly. When a deep cell j (DC, in red) is in contact (green lines) with a margin yolk membrane (MYM, orange) particle i, a "pushing force" $F_{ij}^{\text{m:D},\parallel}$ is calculated to estimate the mechanical pressure exerted by j on the margin at the cellular level. If this force exceeds a certain "resistance threshold" $\theta_{\text{m},\parallel}$, the MYM particle loses its marginal properties, and transmits it to one or several regular YM particle(s) at a more vegetal latitude. c: Schema describing the pushing force exerted by DC particle j over MYM cell i. The pushing force is non-zero only if the distance between the positions of j and i projected on the tangential vector $\vec{U}_{\text{ym},i}^{\parallel}$ (not shown) is smaller than the equilibrium distance $r_{ij}^{\text{eq},\parallel} = c_{\text{eq}}(R_i + R_{\text{ym}})$. The orange and red circles highlight the radii of cells i and j respectively. (For interpretation of the references to color in this figure legend, the reader is referred to the web version of this book.)

6.1.3 GEN: chemical model

The objective of this study is to show that radial intercalation is sufficient to drive epiboly. At the cellular level, the mechanism attributed to the cells is *bipolar protrusion*. We propose two similar means of specifying radial polarization fields through the WTS described in Part 4:

- The first polarization field is specified by the ligand-based polarization mode (a), using a diffusive ligand Q_1 secreted by the EVL. For this ligand, the YSL acts as a sink (Figure 16.16, top embryo).
- The second polarization field is obtained by reversing the sink and source roles, based on another ligand Q_2 secreted by the YSL (Figure 16.16, bottom embryo).

If the interfaces between the EVL deep cells and the YSL deep cells were exactly parallel during epiboly, these two gradients would generate identical polarization fields. This is obviously not the case before 30% epiboly, justifying our choice of two different radial polarization fields. Using the ligand-based polarization mode (a), however, should not be interpreted as an explanation of how a polarization field is actually generated in the embryo. In this

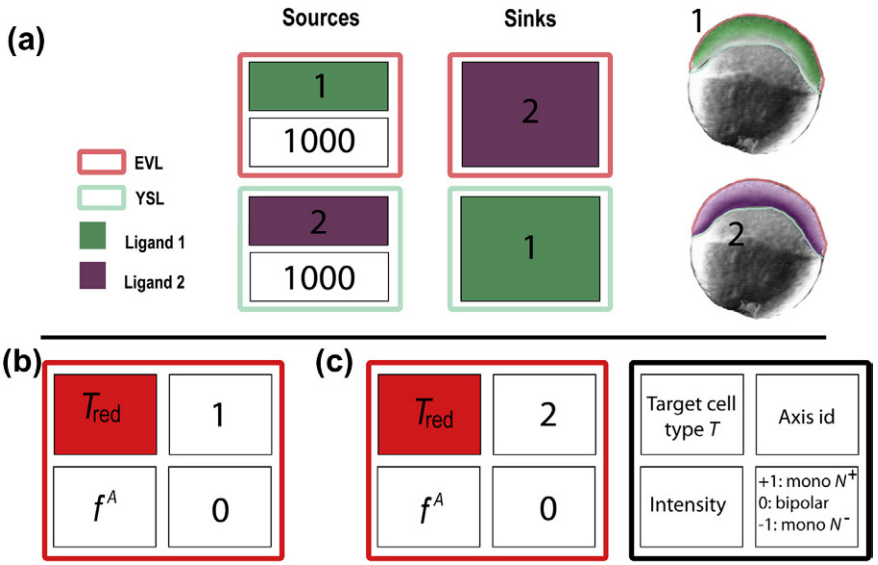

FIGURE 16.16 **Tables for the "Intercalation" case study.** (a) Ligand diffusion table $\mathscr{L}$. Two gradient fields are established by ligand diffusion across the dome region formed by the deep cells. They contribute to the specification of the axes of the polarization: a ligand Q_1 is secreted by the EVL with secretion rate $s_1 = 1000$ and absorbed by the yolk membrane particles, more precisely the YSL. Conversely, a ligand Q_2 is secreted by the YSL with rate $s_2 = 1000$ and absorbed by the EVL. (b,c) Active protrusion tables $\mathscr{A}$. (a) All the cells belonging to the $\mathcal{T}_{\text{red}}$ population exert bipolar protrusions over each other along the polarization axis $\vec{U}_1$ derived from the gradient field of ligand Q_1. (b) The same cells can exert another bipolar protrusion along $\vec{U}_2$ derived from Q_2. In both cases, the intensity of the protrusive force is f^A.

study, we are agnostic with respect to the detailed physico-chemical polarization mechanisms, and only interested in the effects that abstract fields have on cell movements and emerging morphogenetic processes at a macroscopic level.

The polarization fields specified above are highly regular, in any case much less fluctuating than would be the case biologically. To test the effect of a certain amount of stochasticity in these fields, we also introduce a parameter $\lambda_r \in [0, 1]$: if $\lambda_r = 0$, the polarization axes $\vec{U}_i$ are as specified above; if $\lambda_r = 1$, the polarization field is purely random, i.e. for each cell i a random vector $\vec{U}_{r,i}$ is generated every 15 mn of simulation time; intermediate values provide a mix. Thus the effective polarization axis is now $\vec{U}_i^e = \lambda_r \vec{U}_{r,i} + (1 - \lambda_r)\vec{U}_i$, followed by a renormalization step to keep the polarization vector unitary.

6.1.4 *MecaGen: force-chemical coupling model*

Once the polarization fields are established, the protrusive behavior of the cells must be parametrized. For the sake of simplicity, we subsume the deep cell population under one cell type $\mathcal{T}_{\text{red}}$, and postulate homotypic, *bipolar* protrusion forces. Parallel to the pair of polarization fields, we also specify two protrusion rules (Figure 16.16): when the polarization field

originates from the diffusion of ligand Q_1 (resp. Q_2), then protrusions are oriented along axis $\vec{U}_1$ (resp. $\vec{U}_2$). In both cases, the intensity of the protrusive force f^A will be one of the explored parameters. We decided not to vary the passive force coefficients, however (adhesive value $w^{\text{adh}}_{\mathcal{T}_{\text{red}}\mathcal{T}_{\text{red}}}$ and repulsive value w_{rep}), as they counterbalance the effect of f^A, and set them to 1.0 instead.

6.1.5 Extra EVL module

The last factor that we hypothesize to have an influence on the epibolic deformation of the embryo is the *tangential tension* in the EVL. To reflect the fact that the overall surface area of the EVL increases during epiboly, we propose a model that does not intrinsically trigger the spreading but on the contrary resists it. Our model of cell proliferation and growth is controlled by various parameters. The surface area of an EVL cell expands or shrinks depending on the external pressure exerted by its EVL neighbors. If the cell is compressed, i.e. the external pressure is greater than a positive threshold θ^+_{E}, then its lateral radius $R_i^{\text{lat,E}}$ decreases by a ratio γ_{E} (where "E" stands for EVL). On the contrary, if the EVL cell is under tension, i.e. the external pressure is smaller than a negative threshold θ^-_{E}, then $R_i^{\text{lat,E}}$ increases by the same ratio γ_{E}. To control the resistance of the EVL against spreading, we modulate the expansion threshold θ^-_{E}: if it is close to zero, any external tension will trigger expansion and potentially proliferation of the tissue, and the EVL will not resist spreading. Conversely, if the absolute value of θ^-_{E} is high enough, the EVL will not expand or proliferate but will resist spreading. Between these two extremes, we expect that the EVL will exhibit an intermediate degree of resistance, allowing us to decipher its influence on the whole epibolic motion.

6.2 Real embryo and measured data

A qualitative understanding of the macro-scale deformation of the embryo can be derived from Karlstrom and Kane's (1996) "flipbook" of embryogenesis (Karlstrom and Kane 1996) by measuring the macroscopic deformation occurring during epiboly. We extracted 12 images between the oblong stage and the 50% epiboly stage (Figure 16.17), and adjusted this timing in hpf units using the table provided in Karlstrom and Kane (1996) (top left of each frame, second line). We manually annotated the most important landmarks on each image using six dots (see caption).

6.2.1 Real measures

Macroscopic spatial measures were inferred from the singular landmarks described above and consist of the temporal evolution of four absolute *distances* (Figure 16.18, dashed lines): the embryo height from the vegetal pole to animal pole (red dashed line), the margin height from the vegetal pole to the central marginal position (green dashed line), the yolk height from the vegetal pole to the yolk animal pole (blue dashed line), and the margin width from the left to the right marginal positions (yellow dashed line). These measures provide an absolute macroscopic description of the deformation occurring during epiboly. However,

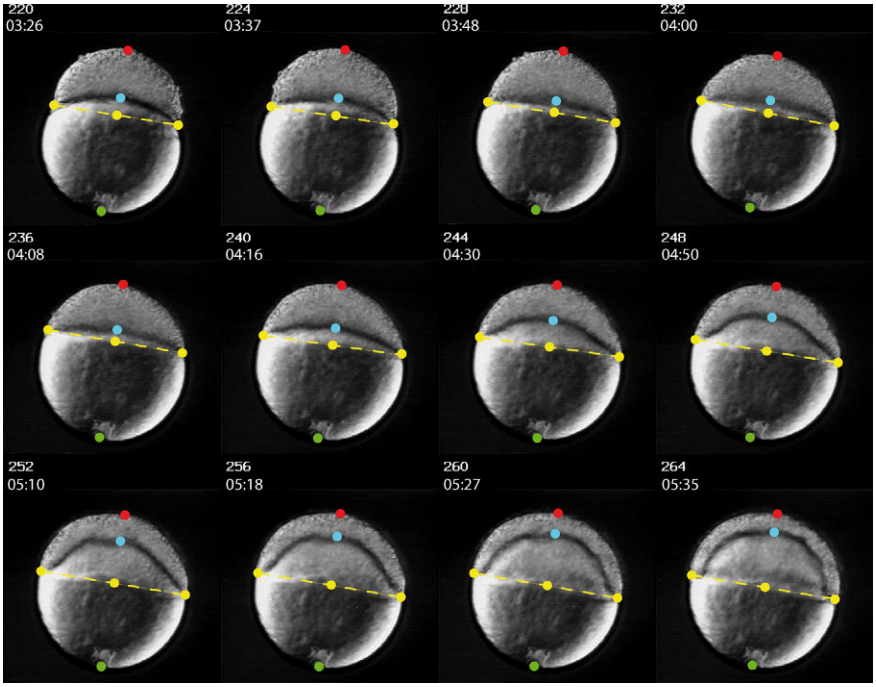

FIGURE 16.17 Macroscopic landmarks of the epibolic deformation from the "flipbook" specimen. Snapshots of the zebrafish development from the oblong stage to 50% epiboly extracted and adapted from the movie by Karlstrom and Kane (1996), with permission. We have manually added colored dots to estimate the macroscopic morphological characteristics of the embryo: red dots signal the animal pole of each embryo, green dots the vegetal pole, blue dots the animal-pole limit of the yolk, and triplets of yellow dots delineate the margin, where the left and right dots identify the external position of the margin and the central one correspond to their averaged projection on the AV axis. The time value displayed below the image id is in hpf units given by Karlstrom and Kane (1996). These timings do not scale linearly with the image ids and have been renormalized. (For interpretation of the references to color in this figure legend, the reader is referred to the web version of this book.)

comparing different embryos, real or simulated, required a normalization of the distances. We chose the embryo height as the baseline, leaving three measures ("e" stands for embryo in the notations):

- the normalized margin height $H_{\mathrm{m}}^{\mathrm{e}}$, obtained by dividing the margin height by the embryo height (green solid line): it characterizes the overall covering of the yolk by the cells, and tends to zero as the tail bud closure proceeds;
- the normalized yolk height $H_{\mathrm{Y}}^{\mathrm{e}}$, obtained by dividing the yolk height by the embryo height (blue solid line): it characterizes the doming of the blastoderm and the bulging of the yolk;
- the embryo *sphericity* coefficient C_{Φ}^{e}, obtained by dividing the margin width by the embryo height (yellow solid line): this value is 1.0 for a spherical embryo, and smaller (resp. greater) for an embryo elongated (resp. flattened) along the AV axis.

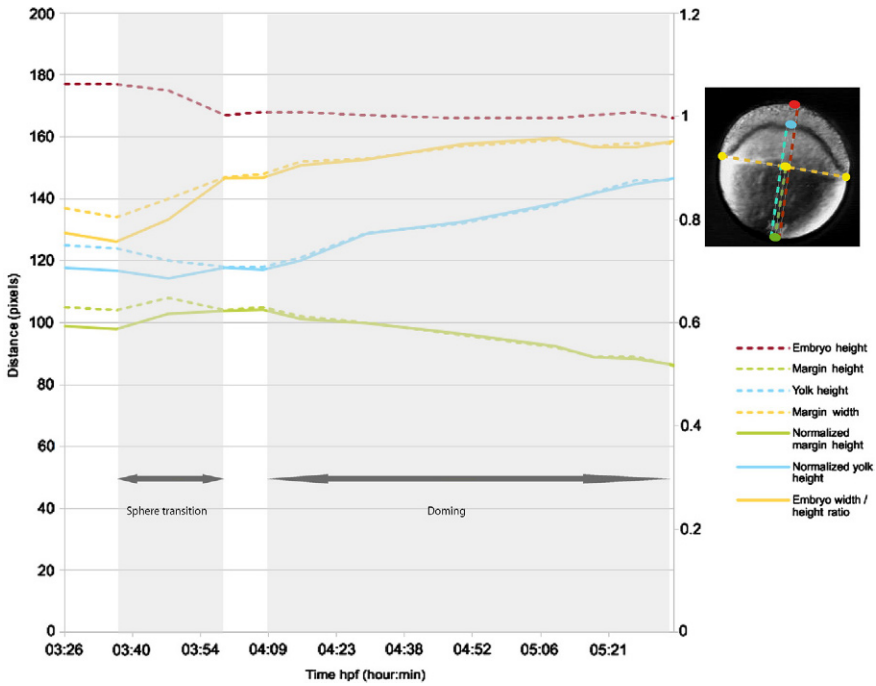

FIGURE 16.18 Macroscopic measures of the epibolic deformation in the "flipbook" specimen. The measures defined by the macroscopic landmarks displayed in Figure 16.17 are shown. The red (top) curve is the plot of the distance between the animal pole (AP) of the embryo and the vegetal pole (VP) of the yolk (embryo height). The green (bottom) curve is the plot of the distance between the projection of the margin on the animal-vegetal (AV) axis and the VP of the yolk (margin height). The blue (next to bottom) curve is distance between the AP of the yolk and the VP of the yolk (yolk height). The yellow (next to top) curve is the lateral distance between the margin positions (margin diameter). The dashed lines give the absolute distance between landmarks in pixels (left ordinate axis). The continuous lines give the normalized distances (right ordinate axis). The normalization is obtained by dividing each value by the current yolk height (i.e. dashed red line). The abscissa gives the time in hpf units. (For interpretation of the references to color in this figure legend, the reader is referred to the web version of this book.)

6.2.2 *Observations*

These simple measures allow distinguishing two macroscopic phases of deformation (gray areas in Figure 16.18): the sphere transition deformation, occurring between 3.6 hpf and 4 hpf in the flipbook, and the doming deformation, starting 8 min later and continuing until about 5.5 hpf. During the sphere transition, the absolute height of the embryo decreases, while its sphericity increases rapidly. The flattening at the sphere stage of the yolk cell-blastoderm interface appears moderate, and it is possible that other specimens behave somewhat differently in this respect (as in Figure 16.14c for example). Additional embryos would be useful to refine this measure (and the other measures as well). The doming transition is accompanied by an important move of the blastoderm margin toward the vegetal pole and an even more important relative displacement of the yolk cell's animal pole, while the overall sphericity slowly increases.

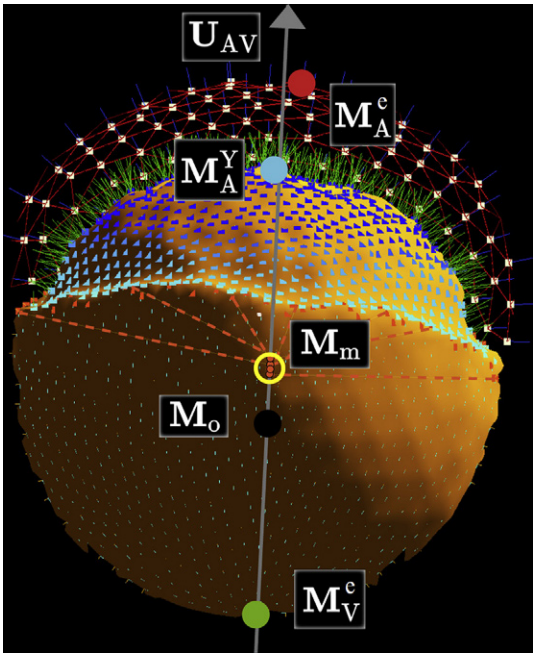

FIGURE 16.19 Macroscopic landmarks of the epibolic deformation in simulated specimens. Landmark dots have been manually added for the purpose of the illustration. They represent the macroscopic landmarks automatically calculated by the simulated measurements. The gray line is the animal-vegetal (AV) axis, *a priori* specified at initialization. The red dot is the embryo animal pole $\mathbf{M}_A^e$, the blue dot is the yolk animal pole $\mathbf{M}_A^Y$, the black dot is the embryo center $\mathbf{M}_o$, the green dot is the embryo vegetal pole $\mathbf{M}_V^e$, the orange dot is the margin "level" $\mathbf{M}_m$, i.e. the average of all the projections of margin yolk membrane particles (small orange circles) on the AV axis (only a few of these particles are displayed). Note that the positions of the yolk animal pole, embryo animal pole, and embryo vegetal pole are never exactly aligned on the AV axis as they must each coincide with a particle's center. The deep cells are not displayed here, leaving a carved out domain between the yolk cell and the EVL. (For interpretation of the references to color in this figure legend, the reader is referred to the web version of this book.)

6.3 Simulated embryo and first comparisons

6.3.1 Simulated measures

In contrast with 2D images of real specimens, the simulated embryo requires automated measurements adapted to its 3D structure. Here, they were calculated in reference to the AV axis and a particular point $\mathbf{M}_o$ in the center of the embryo (in this section, we use upright boldface notation for 3D coordinates and vectors). The unitary vector of the AV axis, denoted by $\mathbf{U}_{AV}$, was specified a priori in the initial conditions (Figure 16.19). The embryo's center $\mathbf{M}_o$ was calculated and updated at each simulation step by averaging the positions of the yolk membrane (ym) and yolk interior (yi) particles:

$$\mathbf{M}_o = \frac{1}{N_{yi} + N_{ym}} \left(\sum_{i=0}^{N_{yi}-1} \mathbf{X}_{yi,i} + \sum_{i=0}^{N_{ym}-1} \mathbf{X}_{ym,i} \right) \tag{16.15}$$

where $\mathbf{X}_{\mathrm{yi},i}$ (resp. $\mathbf{X}_{\mathrm{ym},i}$) is the position of yolk interior (resp. yolk membrane) particle i and N_{yi} (resp. N_{ym}) is the total number of yolk interior (resp. yolk membrane) particles.

The embryo vegetal pole $\mathbf{M}_{\mathrm{V}}^{\mathrm{e}}$, embryo animal pole $\mathbf{M}_{\mathrm{A}}^{\mathrm{e}}$, and yolk animal pole $\mathbf{M}_{\mathrm{A}}^{\mathrm{Y}}$ were obtained by calculating the dot product between $\mathbf{U}_{\mathrm{AV}}$ and each ym or EVL particle's relative position with respect to the center, then selecting the position that realizes the maximum (farthest value in the positive direction) or minimum (farthest value in the negative direction) of this product:

$$\mathbf{M}_{\mathrm{V}}^{\mathrm{e}} = \underset{\mathbf{X}_{\mathrm{ym},i} \in \mathcal{S}_{\mathrm{ym}}}{\arg\min} \left(\left(\mathbf{X}_{\mathrm{ym},i} - \mathbf{M}_{\mathrm{o}} \right) \cdot \mathbf{U}_{\mathrm{AV}} \right) \tag{16.16}$$

$$\mathbf{M}_{\mathrm{A}}^{\mathrm{e}} = \underset{\mathbf{X}_{\mathrm{E},i} \in \mathcal{S}_{\mathrm{E}}}{\arg\max} \left(\left(\mathbf{X}_{\mathrm{E},i} - \mathbf{M}_{\mathrm{o}} \right) \cdot \mathbf{U}_{\mathrm{AV}} \right) \tag{16.17}$$

$$\mathbf{M}_{\mathrm{A}}^{\mathrm{Y}} = \underset{\mathbf{X}_{\mathrm{ym},i} \in \mathcal{S}_{\mathrm{ym}}}{\arg\max} \left(\left(\mathbf{X}_{\mathrm{ym},i} - \mathbf{M}_{\mathrm{o}} \right) \cdot \mathbf{U}_{\mathrm{AV}} \right) \tag{16.18}$$

where $\mathcal{S}_{\mathrm{ym}}$ is the set of yolk membrane particles' position and $\mathcal{S}_{\mathrm{E}}$ is the set of EVL cell particles' position. The projection of the margin on the AV axis, denoted by $\mathbf{M}_{\mathrm{m}}$, was obtained by averaging the point projections of all the margin yolk membrane (MYM) particles onto the AV axis:

$$\mathbf{M}_{\mathrm{m}} = \mathbf{M}_{\mathrm{o}} + \frac{1}{N_{\mathrm{m}}} \sum_{i=0}^{N_{\mathrm{m}}-1} \left(\left(\mathbf{X}_{\mathrm{m},i} - \mathbf{M}_{\mathrm{o}} \right) \cdot \mathbf{U}_{\mathrm{AV}} \right) \mathbf{U}_{\mathrm{AV}} \tag{16.19}$$

where $\mathbf{X}_{\mathrm{m},i}$ is the position of MYM particle i and N_{m} is the number of MYM particles. Finally, the simulated embryo width W was set to twice the average of the radii defined by the distances between the MYM particles and their common projection $\mathbf{M}_{\mathrm{m}}$:

$$W = \frac{2}{N_{\mathrm{m}}} \sum_{i=0}^{N_{\mathrm{m}}-1} \left\| \mathbf{X}_{\mathrm{m},i} - \mathbf{M}_{\mathrm{m}} \right\| \tag{16.20}$$

Similarly to the real specimen, we could then define the same macroscopic measures of epibolic deformation on the simulated embryo (indicated by "s,") i.e. the normalized margin height $H_{\mathrm{m}}^{\mathrm{s}}$, the normalized yolk height $H_{\mathrm{Y}}^{\mathrm{s}}$, and the sphericity ratio C_{Φ}^{s}:

$$H_{\mathrm{m}}^{\mathrm{s}} = \frac{\left\| \mathbf{M}_{\mathrm{m}} - \mathbf{M}_{\mathrm{V}}^{\mathrm{e}} \right\|}{\left\| \mathbf{M}_{\mathrm{A}}^{\mathrm{e}} - \mathbf{M}_{\mathrm{V}}^{\mathrm{e}} \right\|}, \quad H_{\mathrm{Y}}^{\mathrm{s}} = \frac{\left\| \mathbf{M}_{\mathrm{A}}^{\mathrm{Y}} - \mathbf{M}_{\mathrm{V}}^{\mathrm{e}} \right\|}{\left\| \mathbf{M}_{\mathrm{A}}^{\mathrm{e}} - \mathbf{M}_{\mathrm{V}}^{\mathrm{e}} \right\|}, \quad C_{\Phi}^{\mathrm{s}} = \frac{W}{\left\| \mathbf{M}_{\mathrm{A}}^{\mathrm{e}} - \mathbf{M}_{\mathrm{V}}^{\mathrm{e}} \right\|} \tag{16.21}$$

6.3.2 Preliminary results

Judging by Figure 16.20, our first observation was that the deep cells' active protrusive behavior seemed sufficient to drive the embryo's deformation during epiboly in the context of the simulation. The temporal evolution of the above macroscopic measures fits reasonably

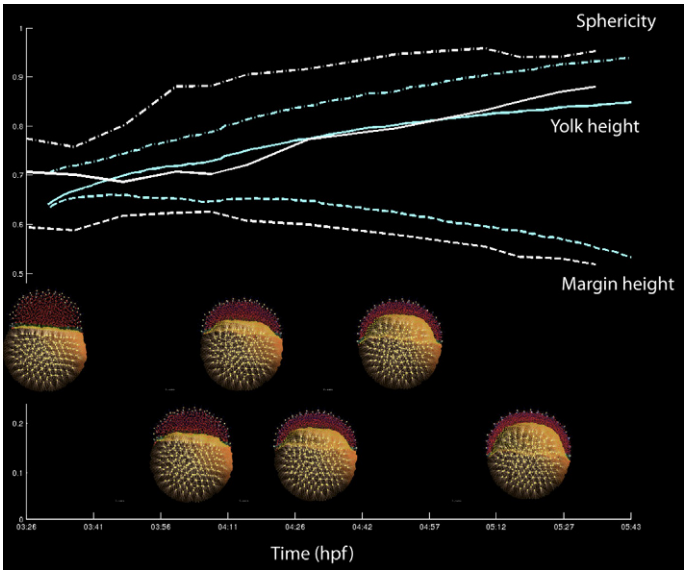

FIGURE 16.20 Macroscopic measures of the epibolic deformation in a simulated specimen. Six snapshots corresponding to different stages of a simulated embryo are displayed along with the temporal evolution of the corresponding macroscopic measures (blue), compared with the flipbook measures (white). Sphericity is represented by the dash-dot lines, normalized yolk height by the solid lines, and normalized margin height by the dashed lines. The embryos' positions correspond approximately to the snapshot times in abscissa. The simulated embryo parameters are: ligand source Q_2 on the yolk, $\theta_{m,\|} = 5.33, \lambda_r = 0, \theta_E^- = 56.67$, and $f^A = 3556$. (For interpretation of the references to color in this figure legend, the reader is referred to the web version of this book.)

well the data extracted from the flipbook. The main discrepancy is the apparent lack of sphere stage transition leading to a spherical morphology during the first hour. We did not observe the characteristic phase of increased sphericity concomitant with a *statu quo* for the normalized yolk and margin heights. In the simulated embryo's trajectory, the early increase of sphericity is always simultaneous with the decrease of at least one of the other macroscopic measures. A possible explanation could be that the initialization of the simulation is not close enough to the real high stage, with a yolk/deep cell interface already presenting a flat shape in the simulation.

6.4 Parameter exploration and validation

6.4.1 Fitness function and parameter space

After studying one virtual embryo under a fixed set of parameters, we proceeded to a broader exploration of parameter space to assess the validity of our simulations and model. For this, we designed a global *fitness function F* to fully automate the quantitative comparison between the simulated embryo and the flipbook specimen. Building upon the above

measures, this function is the average of three objective subfunctions: a normalized margin height function F_{m}; a normalized yolk height function F_{Y}; and a sphericity function F_{Φ}:

$$F = \frac{1}{3}(F_{\mathrm{m}} + F_{\mathrm{Y}} + F_{\Phi}), \quad \text{with}$$
$$F_{\mathrm{m}} = \sum_{t=t_1}^{t_{12}} \left|H_{\mathrm{m}}^{\mathrm{s}}(t) - H_{\mathrm{m}}^{\mathrm{e}}(t)\right|, \quad F_{\mathrm{Y}} = \sum_{t=t_1}^{t_{12}} \left|H_{\mathrm{Y}}^{\mathrm{s}}(t) - H_{\mathrm{Y}}^{\mathrm{e}}(t)\right|, \quad F_{\Phi} = \sum_{t=t_1}^{t_{12}} \left|C_{\Phi}^{\mathrm{s}}(t) - C_{\Phi}^{\mathrm{e}}(t)\right| \tag{16.22}$$

where $t_1 \ldots t_{12}$ are the timings of the 12 images extracted from the flipbook specimen (Figure 16.17). The contribution of each objective function is not individually normalized as these functions represent differences of previously normalized measures.

We explored a five-dimensional parameter space with the following axes: (1) the type of polarization field: EVL-origin or YSL-origin; (2) the margin resistance $\theta_{\mathrm{m},\|}$; (3) the stochasticity of the polarization field controlled by λ_r; (4) the EVL resistance to external tension, controlled by θ_{E}^{-}; and (5) the intensity of the protrusion force f^A. This space was regularly sampled over the range and cardinalities shown in Figure 16.21.

6.4.2 Results

A number of insights could be gained from an analysis of the fitness landscape. A general trend is that the protrusive force intensity f^A and the randomness factor λ_r have counterbalancing effects. A higher protrusive force coupled with a higher random factor produces a fitness level similar to a lower force coupled with a lower randomness, as indicated by the isolines of Figure 16.22. The profile of the isolines reveals the relationship between both parameters: it appears to be supralinear, since an increase of f^A requires an exponential increase of λ_r to be counterbalanced.

For couples of parameters (f^A, λ_r) situated below the isoline passing through coordinates (2,000, 0.05), we did not observe any macroscopic epiboly behavior. We could however qualitatively distinguish different microscopic behaviors in this area: for low levels f^A, the lack of epibolic deformation is due to the lack of intercalating behavior at the cellular level; on the contrary, for high levels of f^A and λ_r, the cells start intercalating inefficiently, with cells sliding

	Min.	Max.	Cardinality	Unit
source	1	2	2	-
$\theta_{\mathrm{m},\|}$	1	40	10	N
λ_r	0	0.1	10	-
θ_{E}^{-}	10	150	10	$\mathrm{N.m^{-2}}$
f^A	0	8000	10	N

FIGURE 16.21 **Range, cardinalities, and units of the five parameters explored in this case study.**

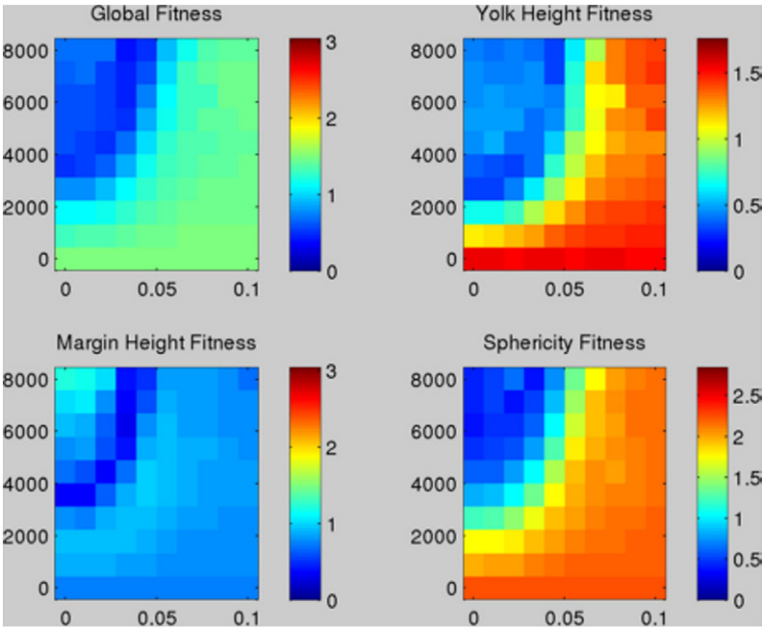

FIGURE 16.22 Fitness landscapes as a function of the random parameter λ_r and the protrusive force intensity parameter f^A. Top Left: global fitness function. Top Right: normalized yolk height objective function F_Y. Bottom Left: normalized margin height function F_m. Bottom Right: sphericity objective function F_Φ. On each plot, the random parameter λ_r is shown in abscissa and the protrusive force intensity f^A in ordinate. The color maps scale between zero and the maximum value of the fitness landscape that they are associated with (to the left).

on each other in a fluid-like manner, and tissue cohesion is lost. This behavior is due to an inequality between the active and passive forces in favor of the protrusive forces.

Further study of these mechanisms would require a preliminary calibration between both types of forces to ensure that these behaviors do not occur. In the following, we performed an a posteriori calibration of f^A at value 3555. Eliminating the f^A dimension allowed a 4D visualization of the fitness landscapes (Figure 16.23) and their mutual comparisons in both polarization scenarios.

Another noticeable general trend was the penalizing effect of the polarization field randomness: all objective functions perform poorly for high λ_r values (top slice of 3D charts). The only exception concerned the normalized margin height measure F_m, which tempered this effect when conjugated with low EVL resistance to tension θ_E^-, and low margin resistance to deep cells' pressure $\theta_{m,\|}$ (Figure 16.23a). Observations of the simulated phenotypes in this particular domain showed that the relaxed state of the EVL and margin, coupled with the low efficiency of the deep cells' protrusive activity (due to high randomness), produced a slight move of the margin toward the vegetal pole along with a de-flattening of the yolk/deep cells interface.

This observation stresses the importance of the embryo's external tension (EVL+Margin) in the shaping of the cellular domain. We also noted that in the scenario of the EVL as a ligand

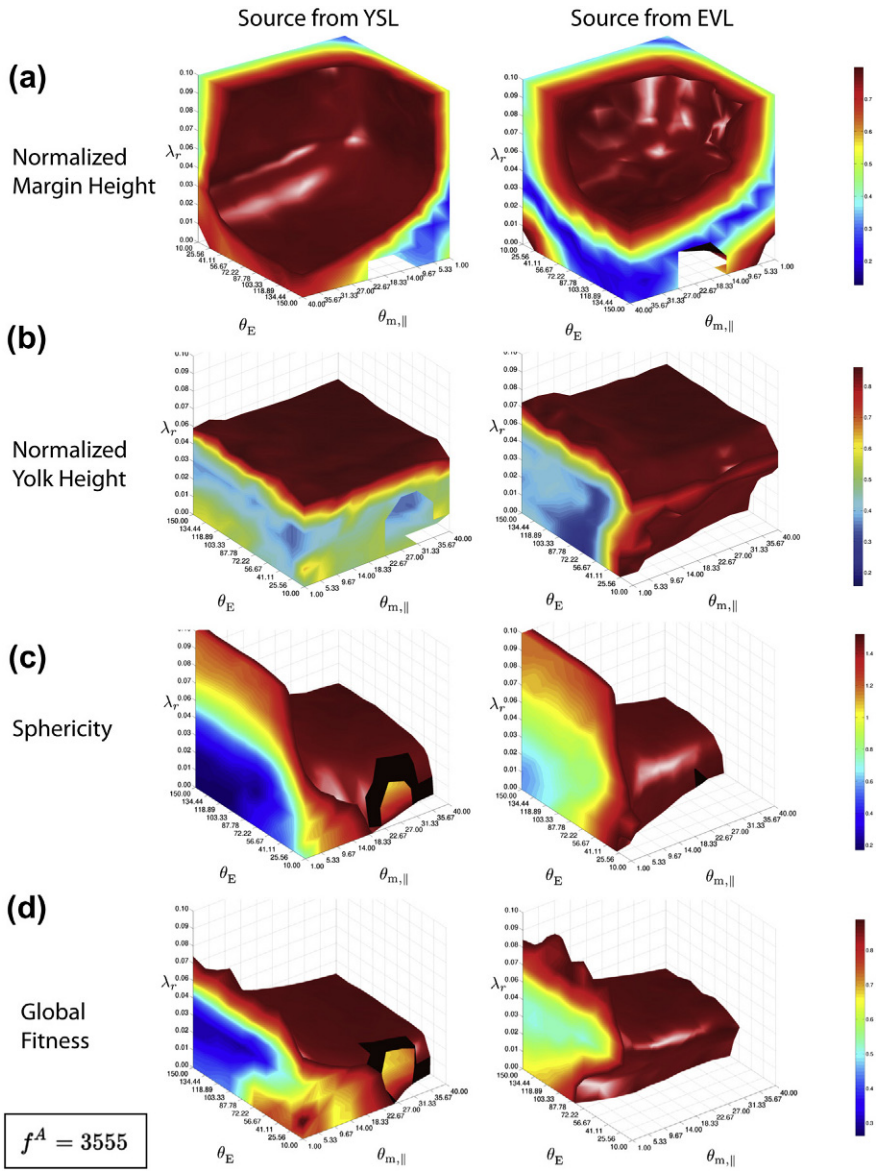

FIGURE 16.23 3D plots of the objective and global fitness functions. For all simulations, the protrusive force intensity f^A has been set to 3555. The vertical axis indicates the random parameter λ_r, the depth axis indicates the threshold controlling the EVL resistance θ_E^-, and the horizontal axis indicates the margin resistance threshold $\theta_{m,\|}$. (a) 3D plot of the normalized margin height objective function F_m. The isosurface represents the best fitness volume (threshold 0.79). This 3D objective function landscape has been rotated, unlike the following plots, to show a better angle of view. (b) 3D plot of the normalized yolk height objective function F_Y. The threshold of the isosurface is set to 0.86. (c) 3D plot of the sphericity objective function F_Φ. The threshold of the isosurface is set to 1.52. (d) 3D plot of the global fitness function F. The threshold of the isosurface is set to 0.88.

source (value 1), the EVL's topology became more irregular. There is feedback coupling between the perturbation of the polarization field, disorienting the deep cells, and the disorganization of the EVL, which in turn perturbs the polarization field. Both yolk height F_Y and sphericity measure F_Φ performed badly as yolk bulging did not occur.

At the opposite side of the parameter spectrum, i.e. low polarization randomness λ_r and high EVL and margin resistances, θ_E^- and $\theta_{m,\|}$, deep cell intercalation gains in efficiency but is blocked by the margin, preventing them to spread over the yolk. Interestingly, the two polarization scenarios offer alternative behaviors in response to this abnormal condition. In the YSL-based field, intercalation exerts a spreading force that deforms the overlying EVL, while this deformation is much more important in the EVL-based field, where the epiboly's spreading triggers a wrenching of the blastoderm from the yolk surface area. This pathological behavior was not expected and can be explained by an inadequacy of the intensity of the forces, without damping induced by random polarization. Obviously, both F_Y and F_Φ penalize the EVL ligand scenario, compared to the YSL one (Figure 16.23b and c, bottom right corner of the cubes).

Another dramatic effect was obtained if a perfectly efficient intercalation, i.e. with no axis randomness, was happening together with strong EVL resistance θ_E^- and weak margin resistance $\theta_{m,\|}$. The previous scenario happened again, i.e. the EVL blocked the spreading of the deep cells, except at some point when the margin still received pressure that made it move toward the vegetal pole, pulling the yolk membrane toward the animal pole. The accumulating yolk membrane ended up being rolled in a unrealistic fashion, stretching the inner yolk membrane particles, and finally allowing the strongly intercalating deep cells to perforate the yolk membrane and penetrate into the yolk.

The last example of aberrant development was detected by measure F_m, when the margin was located too far toward the vegetal pole (Figure 16.23a, bottom right). Yet, the other two measures, F_Y and F_Φ, evaluated the developmental trajectory of the embryo as excellent (Figure 16.23b and c, bottom left corner). This mischaracterization of an abnormal state highlights the difficulty of predicting the behavior of a simulated model.

6.5 Tentative conclusion

Altogether, the simulations conducted in this case study seem to validate the hypothesis that individual cell protrusive activity is sufficient to drive epiboly until the 50% stage. We have pointed out, however, the absence of sphere stage transition, i.e. from the so-called "high stage" to a more spherical shape presenting a flat interface between the yolk and the blastoderm. In the simulated embryos, early increasing sphericity always comes together with a progression of the embryo margin toward the yolk. This may be due to the fact that the initialization of the simulation does not sufficiently resemble the real high stage, as the yolk/deep-cell interface already presents a flat shape in the simulation.

Another interpretation is that additional mechanisms are missing in the explored parameter space, such as a different organization of the polarization field or new behavioral rules in the different compartments of the embryo. In particular, to better characterize the first epiboly episode and capture the effective properties of cell motility, we would need more precise measurements of the individual epibolic behaviors at the cellular level, not just global geometric criteria.

7 DISCUSSION

The "right" mesoscopic level: The most striking characteristic of multicellular systems is their extreme *heterogeneity* of properties and behaviors. As Henri Atlan metaphorically stated through his famous book title "Between Crystal and Smoke" (Atlan 1979), the structure of living matter is somewhere between a highly regularly organized state and a highly randomly disorganized state. Accordingly, the best level to model the morphogenesis of multicellular organisms resides between the macroscopic level, where global mathematical regularities are too constrained and not expressive enough, and the microscopic level, where molecular dynamics is too complex and uncontrollable. Continuous equations must be coupled with discrete local rules, and this necessitates a characterization of the diversity of the underlying cell types and behaviors. A hybrid approach requires a discrete representation of the tissue based on individual components. In our own study of early embryo development, we chose the single-cell level as it allows this local description of cell properties in relatively simple terms. Two criteria led us to make particular choices for the cell biomechanics and the genetic regulation and molecular signaling: the similarities between the variables involved in the model and the observations/concepts produced by the embryologists, on the one hand; and the simplicity of the description leading to a manageable number of parameters, on the other hand. This should not only allow computationally feasible simulations by today's standards but, most importantly, a biologically meaningful interpretation of their outcome.

Portability to other animal models: The MecaGen project was envisioned as a generic modeling platform for all types of animal development. Its foundational principles should be applicable to any multicellular system combining biomechanics with genetic regulation and molecular signaling. The next step in the development of this platform is to expand its cell behavior ontology (CBO) to integrate other types of epithelial and mesenchymal behaviors. In the epithelial case, not many improvements should be needed to fulfill this objective. The adhesion coefficient of "lateral" neighborhood links could be increased and epithelial behaviors, including apical constriction and active intercalation in epithelial layers, should allow the platform to simulate monolayered embryos such as *Drosophila* or sea urchin. This being said, the current MecaGen implementation is not compatible with every animal cell behavior either. Its major limitation resides in the single-particle cell abstraction, which is not adapted to cellular shapes that depart greatly from spheroids or cuboids. Other types of animal morphogenesis rely greatly on cell elongation, such as *Phallusia mammillata* or nematodes. In those cases, an ellipsoid particle model such as Palsson's (Palsson 2001) would provide a reasonable solution for asymmetric cells. In later stages of vertebrate development, too, cells differentiate into extremely stretched shapes such as muscle cells, for which the single-particle framework is clearly inappropriate.

Toward an "evo-devo" perspective: Once the MECA and GEN parts of the model are finally connected and their dynamics truly coupled, without WTS shortcut, a promising extension of this work will be its application to "evolutionary developmental" questions. Evo-devo does not generally aim at directly comparing simulated phenotypes and real embryos but rather asking how evolution is able to generate new structures and behaviors at the level of

the whole embryo. This would involve modeling and simulating an even higher level of organization, in which the whole embryo behaves and potentially interacts with its environment. It can be seen as another way to explore the model's parameter space without isolating the developmental trajectories around a target phenotype (zebrafish in this chapter). The evaluation would emerge from a Darwinian selection process in an artificial environment—whether by survival or reproduction of particular behaviors. A particularly fascinating exploration would be to start from a simple individual organism such as the *urbilaterian*, a hypothetical ancestor of all animals exhibiting bilateral symmetry (Erwin and Davidson 2002; Hejnol and Martindale 2008), and guide its evolution through mutation of its gene regulatory networks toward multiple descendant species. To our knowledge, no computational evo-devo study has proposed a developmental model presenting as many similarities with real biological systems as MecaGen does. It would be a great opportunity to better decipher and understand the evolutionary forces that drive the diversity of life.

References

Coen, E. (1999). *The Art of Genes. How Organisms Make Themselves*. Oxford University Press on Demand.

Hopwood, N. (2008). Embryology. *Cambridge History of Science* **6.**

Lawrence, P. A., and Levine, M. (2006). Mosaic and regulative development: two faces of one coin. *Curr. Biol.* **16**(7):R236–R239.

Nüsslein-Volhard, C., and Wieschaus, E. (1980). Mutations affecting segment number and polarity in Drosophila. *Nature* **287**(5785):795–801.

Nüsslein-Volhard, C. (2012). The zebrafish issue of Development. *Development* **139**(22):4099–4103.

Arnone, M. I., and Davidson, E. H. (1997). The hardwiring of development: organization and function of genomic regulatory systems. *Development* **124**(10):1851–1864.

Chan, T.-M., Longabaugh, W., Bolouri, H., Chen, H.-L., Tseng, W.-F., Chao, C.-H., Jang, T.-H., Lin, Y.-I., Hung, S.-C., Wang, H.-D., and Yuh, C.-H. (2009). Developmental gene regulatory networks in the zebrafish embryo. *Biochim. biophys. Acta.* **1789**(4):279–298.

Pelegri, F. (2003). Maternal factors in zebrafish development. *Develop. Dyn. : An official publication of the American Association of Anatomists* **228**(3):535–554.

Gavis, E. R., and Lehmann, R. (1992). Localization of nanos RNA controls embryonic polarity. *Cell* **71**(2):301–313.

Keller, R. (2012). Physical biology returns to morphogenesis. *Science* **338**(6104):201–203.

Steinberg, M. S. (1962). On the mechanism of tissue reconstruction by dissociated cells. I. Population kinetics, differential adhesiveness. and the absence of directed migration. *Proc. Natl. Acad. Sci. USA* **48**:1577–1582.

von Dassow, M., and Davidson, L. A. (2011). Physics and the canalization of morphogenesis: a grand challenge in organismal biology. *Phys. Biol.* **8**(4):045002.

Turing, A. M. (1952). The chemical basis of morphogenesis. *Philos. Trans. R. Soc. Lond. B, Biol. Sci.* **237**(641):37–72.

Gierer, A., and Meinhardt, H. (1972). A theory of biological pattern formation. *Biol. Cybern.* **12**(1):30–39.

Meinhardt, H., and Gierer, A. (1974). Applications of a theory of biological pattern formation based on lateral inhibition. *J. Cell Sci.* **15**(2):321–346.

Young, D. A. (1984). A local activator-inhibitor model of vertebrate skin patterns. *Math. Biosci.* **72**(1):51–58.

Kondo, S., and Miura, T. (2010). Reaction-diffusion model as a framework for understanding biological pattern formation. *Science* **329**(5999):1616–1620.

Bieler, J., Pozzorini, C., and Naef, F. (2011). Whole-embryo modeling of early segmentation in Drosophila identifies robust and fragile expression domains. *Biophys. J.* **101**(2):287–296.

Inaba, M., Yamanaka, H., and Kondo, S. (2012). Pigment pattern formation by contact-dependent depolarization. *Science* **335**(6069):677.

Wolpert, L. (1969). Positional information and the spatial pattern of cellular differentiation. *J. Theor. Biol.* **25**(1):1.

Wolpert, L. (2011). Positional information and patterning revisited. *J. Theor. Biol.* **269**(1):359–365.

Lawrence, P. A. (2001). Morphogens: how big is the big picture?. *Nat. Cell Biol.* **3**(7):E151–4.
Lander, A. D., Nie, Q., and Wan, F. Y. M. (2002). Do morphogen gradients arise by diffusion?. *Develop. cell* **2**(6):785–796.
Tabata, T., and Takei, Y. (2004). Morphogens, their identification and regulation. *Development* **131**(4):703–712.
Kicheva, A., Bollenbach, T., Wartlick, O., Jülicher, F., and González-Gaitán, M. (2012). Investigating the principles of morphogen gradient formation: from tissues to cells. *Curr. opin. Genet. Develop.* 1–6.
Eggenberger, P. (1997). Evolving morphologies of simulated 3D organisms based on differential gene expression. In *Proceedings of the Fourth European Conference on Artificial Life*, pp. 205–213.
Kumar, S., and Bentley, P. (2003). Biologically inspired evolutionary development. In *Evolvable Systems: From Biology to Hardware*, pp. 57–68.
Doursat, R. (2006). The growing canvas of biological development: multiscale pattern generation on an expanding lattice of gene regulatory nets. *InterJournal: Complex Systems 1809*
Barkai, N., and Shilo, B.-Z. (2009). Robust generation and decoding of morphogen gradients. *Cold Spring Harb. Perspect. Biol.* **1**(5):a001990.
Kauffman, S. (1969). Homeostasis and differentiation in random genetic control networks. *Nature* **224**(5215):177–178.
Reinitz, J., and Sharp, D. (1995). Mechanism of eve stripe formation. *Mech. Develop.* **49**(1):133.
Rolland-Lagan, A., Paquette, M., Tweedle, V., and Akimenko, M. (2012). Morphogen-based simulation model of ray growth and joint patterning during fin development and regeneration. *Development* **139**:1–10.
Gibson, M. C., Patel, A. B., Nagpal, R., and Perrimon, N. (2006). The emergence of geometric order in proliferating metazoan epithelia. *Nature* **442**(7106):1038–1041.
Farhadifar, R., Röper, J., Aigouy, B., Eaton, S., and Jülicher, F. (2007). The influence of cell mechanics, cell-cell interactions, and proliferation on epithelial packing. *Curr. Biol.* **17**(24):2095–2104.
Sandersius, S., Chuai, M., Weijer, C., and Newman, T. (2011). Correlating Cell Behavior with Tissue Topology in Embryonic Epithelia. *PLoS One* **6**(4):e18081.
Graner, F., and Glazier, J. (1992). Simulation of biological cell sorting using a two-dimensional extended Potts model. *Phys. Rev. Lett.* **69**(13):2013–2016.
Glazier, J., and Graner, F. (1993). Simulation of the differential adhesion driven rearrangement of biological cells. *Phys. Rev. E* **47**(3):2128–2154.
Brodland, G. W., and Chen, H. H. (2000). The mechanics of heterotypic cell aggregates: insights from computer simulations. *J. Biomech. Eng.* **122**(4):402–407.
Landsberg, K. P., Farhadifar, R., Ranft, J., Umetsu, D., Widmann, T. J., Bittig, T., Said, A., Jülicher, F., and Dahmann, C. (2009). Increased cell bond tension governs cell sorting at the drosophila anteroposterior compartment boundary. *Curr. Biol.* **19**(22):1950–1955.
Aliee, M., Röper, J.-C., Landsberg, K. P., Pentzold, C., Widmann, T. J., Jülicher, F., and Dahmann, C. (2012). Physical mechanisms shaping the drosophila dorsoventral compartment boundary. *Curr. Biol.* 1–10.
Beatrici, C. P., and Brunnet, L. G. (2011). Cell sorting based on motility differences. *Phys. Rev. E* **84**(3 Pt 1):031927.
Foty, R., and Steinberg, M. (2005). The differential adhesion hypothesis: a direct evaluation. *Develop. Biol.* **278**(1):255–263.
Zhang, Y., Thomas, G. L., Swat, M., Shirinifard, A., and Glazier, J. A. (2011). Computer Simulations of Cell Sorting Due to Differential Adhesion. *PLoS One* **6**(10):e24999.
Maitre, J. L., Berthoumieux, H., Krens, S. F. G., Salbreux, G., Jülicher, F., Paluch, E., and Heisenberg, C.-P. (2012). Adhesion Functions in Cell Sorting by Mechanically Coupling the Cortices of Adhering Cells. *Science* **338**(6104):253–256.
Blanchard, G. B., and Adams, R. J. (2011). Measuring the multi-scale integration of mechanical forces during morphogenesis. *Curr. Opin. Genet. Develop.* 1–11.
van Leeuwen, I. M. M., Mirams, G. R., Walter, A., Fletcher, A., Murray, P., Osborne, J., Varma, S., Young, S. J., Cooper, J., Doyle, B., Pitt-Francis, J., Momtahan, L., Pathmanathan, P., Whiteley, J. P., Chapman, S. J., Gavaghan, D. J., Jensen, O. E., King, J. R., Maini, P. K., Waters, S. L., and Byrne, H. M. (2009). An integrative computational model for intestinal tissue renewal. *Cell Prolif.* **42**(5):617–636.
Grima, R. (2008). Multiscale modeling of biological pattern formation. *Curr. Top. Develop. Biol.* **81**:435–460.
Little, S. C., and Wieschaus, E. F. (2011). Shifting patterns: merging molecules, morphogens, motility, and methodology. *Develop. cell* **21**(1):2–4.
Izaguirre, J., Chaturvedi, R., Huang, C., Cickovski, T., Coffland, J., Thomas, G., Forgacs, G., Alber, M., Hentschel, G., and Newman, S. (2004). CompuCell, a multi-model framework for simulation of morphogenesis. *Bioinformatics* **20**(7):1129–1137.

Cickovski, T., Aras, K., Swat, M., Merks, R., Glimm, T., Hentschel, H., Alber, M., Glazier, J., Newman, S., and Izaguirre, J. (2007). From genes to organisms via the cell: a problem-solving environment for multicellular development. *Comput. Sci. Eng.* **9**(4):50–60.

Swat, M. H. M., Hester, S. D. S., Balter, A. I. A., Heiland, R. W. R., Zaitlen, B. L. B., and Glazier, J. A. J. (2008). Multicell simulations of development and disease using the CompuCell 3D simulation environment. *Methods Mol. Biol.* **500**:361–428. (Clifton, NJ).

Doursat, R. (2008). Programmable architectures that are complex and self-organized: From morphogenesis to engineering. In *Proceedings of Artificial XI*, pp. 181–188.

Joachimczak, M., and Wróbel, B. (2008). Evo-devo in silico: a model of a gene network regulating multicellular development in 3D space with artificial physics. In *Proceedings of the Eleventh International Conference on the Simulation and Synthesis of Living Systems, Artificial Life XI*, pp. 297–304.

Schramm, L., Jin, Y., and Sendhoff, B. (2011). Emerged coupling of motor control and morphological development in evolution of multi-cellular animats. *Advances in Artificial Life. Darwin Meets von Neumann* 27–34.

Doursat, R., Sánchez, C., Dordea, R., Fourquet, D., and Kowaliw, T. (2012). Embryomorphic engineering: emergent innovation through evolutionary development. In (R. Doursat, H. Sayama, and O. Michel, eds.), *Morphogenetic Engineering: Toward Programmable Complex Systems*. Springer.

Murray, J. D. (2003). *Mathematical biology II: spatial models and biomedical applications*. Springer.

Fleury, V. (2005). An elasto-plastic model of avian gastrulation. *Organogenesis* **2**(1):6–16.

Deutsch, A., and Dormann, S. (). Cellular Automaton Modeling of Biological Pattern Formation. In Characterization, Applications, and Analysis2005. Boston: Birkhauser.

Marée, A., and Hogeweg, P. (2001). How amoeboids self-organize into a fruiting body: multicellular coordination in *Dictyostelium discoideum*. *Proc. Natl. Acad. Sci.* **98**(7):3879.

Schaller, G., and Meyer-Hermann, M. (2004). Kinetic and dynamic Delaunay tetrahedralizations in three dimensions. *Comput. Phys. Commun.* **162**(1):9–23.

Newman, T. J. (2005). Modeling multicellular systems using subcellular elements. *Math. Biosci. Eng.* **2**(3):613–624.

Wilczynski, B., and Furlong, E. E. M. (2010). Challenges for modeling global gene regulatory networks during development: Insights from Drosophila. *Develop. Biol.* **340**(2):161–169.

Ben-Tabou de Leon, S., and Davidson, E. (2009). Modeling the dynamics of transcriptional gene regulatory networks for animal development. *Develop. Biol.* **325**(2):317–328.

Giacomantonio, C. E., and Goodhill, G. J. (2010). A Boolean Model of the Gene Regulatory Network Underlying Mammalian Cortical Area Development. *PLoS Comput. Biol.* **6**(9):e1000936.

Peter, I. S., Faure, E., and Davidson, E. H. (2012). Predictive computation of genomic logic processing functions in embryonic development. *Proc. Natl. Acad. Sci.* **109**(41):16434–16442.

Kojić, N., Huang, A., Chung, E., Ivanović, M., Filipović, N., Kojić, M., and Tschumperlin, D. J. (2010). A 3-D Model of Ligand Transport in a Deforming Extracellular Space. *Biophys. J.* **99**(11):3517–3525.

Thomas, R. R. (1973). Boolean formalization of genetic control circuits. *J. Theor. Biol.* **42**(3):563–585.

Davidson, E. H. (2010). Emerging properties of animal gene regulatory networks. *Nature* **468**(7326):911–920.

Peter, I. S., and Davidson, E. H. (2009). Modularity and design principles in the sea urchin embryo gene regulatory network. *FEBS Lett.* **583**(24):3948–3958.

Davidson, E. H. (2009). Network design principles from the sea urchin embryo. *Curr. Opin. Genet. Develop.* **19**(6):535–540.

Solnica-Krezel, L., and Driever, W. (1994). Microtubule arrays of the zebrafish yolk cell: organization and function during epiboly. *Development* **120**(9):2443–2455.

Karlstrom, R. O., and Kane, D. A. (1996). A flipbook of zebrafish embryogenesis. *Development* **123**:461.

Atlan, Henri (1979). *Entre le cristal et la fumée: essai sur l'organisation du vivant*. Éditions du Seuil.

Palsson, E. (2001). A three-dimensional model of cell movement in multicellular systems. *Future Gener. Comput. Syst.* **17**(7):835–852.

Erwin, D. H., and Davidson, E. H. (2002). The last common bilaterian ancestor. *Development* **129**(13):3021–3032.

Hejnol, A., and Martindale, M. Q. (2008). Acoel development supports a simple planula-like urbilaterian. *Phil. Trans. R. Soc. B: Biol. Sci.* **363**(1496):1493–1501.

Kimmel, C. B., Ballard, W. W., Kimmel, S. R., Ullmann, B., and Schilling, T. F. (1995). Stages of embryonic development of the zebrafish. *Develop. Dyn. : An official publication of the American Association of Anatomists* **203**(3):253–310.